

Final Report: Alignment of Wind Reliability Analysis with Code-Based Equivalent Static Wind Load Methods

Prepared by: Dr. Seymour MJ Spence and Ms. Jieling Jiang
University of Michigan

Sponsor:

- **Magnusson Klemencic Associates (MKA) Foundation**
- **Arup US, Inc.**

MKA Foundation support was cost-shared with:

- CPP Wind Engineering Consultants
- RWDI Consulting Engineers and Scientists
- DeSimone Consulting Engineers
- Walter P. Moore
- Mr. Russell Larsen
- TLSmith Consulting Inc
- SK&A Structural Engineers, PLLC

Project Period: Feb. 01, 2023 - Feb. 29, 2024

Executive Summary

This project aimed to first identify the underlying reasons why wind demands estimated through wind time history analysis have been seen on occasion to exceed demand envelopes estimated from equivalent static wind loads (ESWLs) and secondly to uncover the reasons why initial reliability studies have suggested that there is a discrepancy between the reliabilities obtained from systems designed to comply with current load and resistance factor design (LRFD) procedures for steel and reinforced concrete main wind force resisting systems (MWFRS) and the target reliabilities indicated in Table 1.3-1 of ASCE 7-22.

In the first phase of the project, record-to-record variability was investigated as a possible cause for wind demands estimated from time history analysis exceeding those estimated from ESWLs. Record-to-record variability is a fundamental aspect of any system exposed to stochastic excitation, including structural systems subject to dynamic wind loads. In the past, wind engineering methodologies have typically disregarded this variability by focusing on the expected peak responses, i.e., the average peak response obtained from analyzing the MWFRS for multiple realizations of the dynamic wind loads for each relevant wind speed and direction. Various historical factors have contributed to this state of affairs, including the efficient estimation of expected peaks in the frequency domain for linear elastic systems. However, the growing interest in wind analysis schemes that employ time history analysis, for example, performance-based wind design, can lead to important inconsistencies. Indeed, wind time history analysis is often carried out (for a multitude of reasons) using a single wind record for each critical wind direction. Findings from this phase of the project demonstrate that record-to-record variability can significantly alter the peak responses of the MWFRS. The observed coefficient of variation on peak responses, particularly the demand-to-capacity ratios of critical components, generally falls between 0.1 and 0.3. A formal sensitivity analysis conducted using the Sobol method revealed that record-to-record variability can represent an important source of system uncertainty. This variability in peak responses is accounted for in traditional wind design approaches, which are based on ESWLs, through the use of expected peak values. As would be expected, an analysis of archetype structures revealed that variability around the expected peak can lead to wind responses surpassing the wind demand envelopes estimated from ESWLs. If practical, it is therefore proposed that a suite of wind records be considered for each wind speed

and direction involved in time history analysis. This would allow for the direct estimation of expected peak responses and the variability around this value due to record-to-record variability. If running multiple wind records is computationally prohibitive, using a single record that is appropriately scaled to produce the expected peak of a critical response parameter is recommended. Such considerations are particularly important when conducting nonlinear time history analysis due to its path-dependent nature.

During the project's second phase, the causes behind the apparent discrepancies in the reliability of the MWFRS, designed to comply with current LRFD requirements using ESWL derived from building-specific wind tunnel tests and calibrated to the wind intensities suggested in ASCE 7, were examined. To this end, the reliability of two Risk Category II archetype MWFRS was investigated with the "true" reliabilities of these archetypes estimated through the application of the wind reliability modeling environment, WiRA. To ensure the WiRA models were compliant with the finite element models of the designers of the archetypes, a rigorous QA/QC was carried out. This led to baseline component reliability estimates that appeared to be deficient compared to the target reliabilities suggested in ASCE 7-22 for code-compliant building systems. The influence of modeling choices related to the wind hazard, such as the choice of the wind hazard curve, on the results was examined and was not found to be the root cause of the deficit in reliability. Consequently, the theory supporting the wind reliability estimates used in calibrating LRFD was revisited. It was shown that if wind loads are calibrated using wind effects with mean recurrence intervals (MRIs) that are consistent with those suggested in ASCE 7 for Risk Category II structures, the target reliabilities of Table 1.3-1 will not, in general, be achieved. Consequently, it could be argued that the MRIs for the design winds speeds of ASCE 7 should be multiplied by a coefficient of $\sqrt{1.2}$ before use in design. As noted in [0.1], for Risk Category II buildings in extratropical regions and limit states where "Failure that is not sudden or does not lead to widespread progression of damage", the lack of such a factor can lead to an apparent reliability reduction from 3.0 to around 2.5. Currently, these nuances are lacking in the presentation of Table 1.3-1 of ASCE 7.

In summary, record-to-record variability, i.e., the natural variability in the time history wind load traces given an identical average wind speed and wind direction, was seen to be a contributing factor why wind time history analysis can exceed demand envelopes estimated from ESWLs while the apparent discrepancy between the reliability of structural systems designed using advanced wind analysis procedures and the targets suggested in Table 1.3-1 of ASCE 7 was revealed to be contributed by the loss of an implicit factor that can be interpreted as unduly reducing the MRIs of the design wind speeds (or load effects used to define loading scenarios for use in LRFD or performance-based wind design).

Disclaimer: The results of the second phase of the project must be considered in light of the following limitations:

1. All reliability results were estimated using stochastic simulation and are therefore subject to inevitable statistical error associated with the use of a limited set of samples. The values discussed in this report should therefore be taken as representative but could be in excess or deficit of the true value.
2. All reliability analyses carried out in the second phase of the project do not consider epistemic uncertainties, i.e., systematic or reducible uncertainty, arising from imperfect models. This is important to clarify as building-specific wind tunnel data coupled with dynamic analysis of the system provides a representation with far lower epistemic uncertainty than, for example, the simplified models used to define Table 1.3-1. Strictly speaking, a comprehensive comparison between the target reliabilities of Table 1.3-1 and those obtained from the type of analysis used in the second phase of the project should consider this difference in epistemic uncertainty. Such considerations should be further studied before definitive conclusions are drawn from the results presented in this report.

Bibliography

[0.1] T. P. McAllister, N. Wang, and B. R. Ellingwood. Risk-informed mean recurrence intervals for updated wind maps in ASCE 7-16. *Journal of Structural Engineering*, 144(5):06018001, 2018.

Table of Contents

Executive Summary	ii
Table of Contents	v
List of Tables	vii
List of Figures	viii
1 Phase 1: The importance of record-to-record variability in time history analysis of the MWFRS	1
1.1 Dynamic response framework	2
1.1.1 Overview	2
1.1.2 Mechanical model and elastic solution	2
1.1.3 Stochastic wind load model	4
1.1.4 The archetype buildings	6
1.2 Uncertainty in the DCRs generated by record-to-record variability .	8
1.2.1 Load case	8
1.2.2 Results	8
1.3 Sensitivity analysis	19
1.3.1 Sobol indices	19
1.3.2 Uncertainties and macro parameters	21
1.3.3 Results	23
1.4 Concluding Remarks	26
Bibliography	27
2 Phase 2: Uncovering the reasons behind the apparent discrepancy between target and achieved reliability	30
2.1 Explicit reliability estimation by WiRA	31
2.1.1 The reliability problem	31
2.1.2 Model and load uncertainties	32
2.1.3 Stochastic simulation scheme	34
2.2 Explicit reliability results	35
2.2.1 Problem setup	35
2.2.2 Results	36
2.3 Sensitivity to climatological and aerodynamic modeling choices . . .	43

2.4	Classic reliability estimates and comparison to explicit reliability modeling	44
2.4.1	Reliability calculations underpinning LRFD	44
2.4.2	Comparison to explicit reliability estimates	49
2.5	Concluding remarks	51
Bibliography		53
A Finite element model development and QA/QC		56
A.1	Square steel NYC	56
A.1.1	Modeling approach	56
A.1.2	QA/QC: Column line response comparison	57
A.2	Rectangular Concrete NYC	58
A.2.1	Modeling approach	58
A.2.2	QA/QC: Wall line response comparison	58
B Stochastic wind load model and the Miami archetype		60
B.1	Wind load calibration	60
B.2	Discussion on the Peak DCR	60

List of Tables

1.1	Uncertainties in the gravity and wind loads.	22
1.2	Description of random variables in steel MWFRS.	22
1.3	Description of random variables in reinforced concrete MWFRS.	23
2.1	Distribution parameters used for modeling the uncertainty in the gravity loads.	34
2.2	Values of κ for different wind direction sectors.	36
2.3	NY square steel archetype: LS1 reliability index of the critical component for each wind sector.	38
2.4	NY rectangular concrete core archetype: LS1 reliability index of the critical component for each wind sector.	38
2.5	Distributions of load effects and resistances	47
A.1	NY square steel archetype: natural frequency comparison between the ETABS model of the designers and the OpenSees Navigator and WiRA models of the project (Units: Hz).	57
A.2	NY rectangular concrete core archetype: natural frequency comparison between the ETABS model of the designers and the OpenSees Navigator and WiRA models of the project (Units: Hz).	58

List of Figures

1.1	Archetype buildings.	7
1.2	NY square steel archetype: Maximum DCRs over all load cases of the ESWLS and over all wind directions for the dynamic wind loads.	9
1.3	NY square steel archetype: Maximum of Eq. (1.18) over all elements.	9
1.4	Miami rectangular steel archetype: Maximum DCRs over all load cases of the ESWLS and over all wind directions for the dynamic wind loads.	10
1.5	Miami rectangular steel archetype: Maximum of Eq. (1.18) over all elements (Note: the ratios of this figure should be interpreted with caution as the preliminary dynamic properties used by CPP to estimate the ESWLS differ significantly from those of the final design therefore indicating that the ESWLS would require updating before the results can be deemed representative).	10
1.6	NY rectangular concrete core archetype: Maximum DCRs over all load cases of the ESWLS and over all wind directions for the dynamic wind loads.	11
1.7	NY square steel archetype: Maximum of Eq. (1.18) over all elements.	11
1.8	NY square steel archetype: record-to-record variability for all wind directions and the maximum DCR over all components.	14
1.9	NY square steel archetype: Time history of the critical DCR projection for the component with maximum DCR estimated from the ESWLS.	14
1.10	NY square steel archetype: zoom of the time history of Fig. 1.9 around the maximum DCR (Note: The applied wind loads were linearly ramped using the model outlined in Chapter 2, Eq. (2.6)).	15
1.11	Miami rectangular steel archetype: record-to-record variability for all wind directions and the maximum DCR over all components (Note: the responses estimated from the application of the ESWLS are not reported as the preliminary dynamic properties used by CPP to estimate the ESWLS differ significantly from those of the final design therefore indicating that the ESWLS would require updating before the results can be deemed representative).	16

1.12	NY rectangular concrete core archetype: record-to-record variability for all wind directions and the maximum DCR over all components.	16
1.13	NY square steel archetype: Maximum COV over all components or wind direction.	18
1.14	Miami rectangular steel archetype: Maximum COV over all components or wind direction.	18
1.15	NY rectangular concrete core archetype: Maximum COV over all components or wind direction (components with mean DCR less than 0.1 indicated in gray).	19
1.16	NY square steel archetype: histograms of DCRs for key components.	20
1.17	NY square steel archetype: location of key components.	21
1.18	NY square steel archetype: Total-effect Sobol index for the maximum DCR over and elastic multiplier.	24
1.19	NY square steel archetype: Total-effect Sobol index for the alongwind and acrosswind maximum (over the height of the building) interstory drift.	24
1.20	NY rectangular concrete core archetype: Total-effect Sobol index for the maximum DCR over and elastic multiplier.	25
1.21	NY rectangular concrete core archetype: Total-effect Sobol index for the alongwind and acrosswind maximum (over the height of the building) interstory drift.	25
2.1	NY square steel archetype: histograms of the sampled damping ratios for each sector.	39
2.2	NY square steel archetype: Component reliability (LS1).	40
2.3	NY rectangular concrete core archetype: Component reliability (LS1).	40
2.4	NY square steel archetype: elastic multiplier, S_e , estimated for random damping and a fixed damping of 2% ($S_e < 1.4$ shown).	41
2.5	NY rectangular concrete core archetype: elastic multiplier, S_e , estimated for random damping and a fixed damping of 2% ($S_e < 1.4$ shown).	41
2.6	NY square steel archetype: $S_e < 1$ values vs random damping.	42
2.7	NY rectangular concrete core archetype: $S_e < 1$ values vs random damping.	42
2.8	NY square steel archetype: LS1 reliability difference between AC1 and the baseline case.	44
2.9	NY square steel archetype: LS1 reliability difference between AC2 and the baseline case.	45
2.10	Weibull and Type I distribution curves of the largest 50-year non-directional wind speed.	45
2.11	Reliability index for the simplified reliability case with W_{50}/D_n ranging from 1 to 4 and L_0/D_n ranging from 0 to 1.	48

2.12	Variation of reliability with W_{50}/D_n and DCR_n for $L_0/D_n = 0$ and the simplified reliability model of Section 2.4.1.	50
2.13	Comparison between reliabilities estimated from the simplified model of Section 2.4.1 and those estimated from the WiRA framework of 2.1.	50
2.14	Difference between reliability estimated from the WiRA framework of Section 2.1 and the simple model of Section 2.4.1.	51
A.1	Normalized response comparison for the C1 column line.	57
A.2	Normalized response comparison for the C2 column line.	57
A.3	Normalized response comparison for the C3 column line.	58
A.4	Normalized response comparison for the A1 shear wall.	59
A.5	Normalized response comparison for the B1 shear wall.	59
A.6	Normalized response comparison for the C1 shear wall.	59
B.1	Miami rectangular steel archetype: PSD comparison between the aerodynamic base moments for a wind direction of 200°	61
B.2	Miami rectangular steel archetype: CPSD comparison between the aerodynamic base moments for a wind direction of 200°	62
B.3	Comparison between the target and simulated skewness and kurtosis of the floor loads.	63
B.4	Critical wind demand DCR time history for the component experiencing the maximum DCR under the dynamic wind tunnel load.	64
B.5	PSD of the critical wind demand DCR time histories of Fig. B.4.	64

Chapter 1

Phase 1: The importance of record-to-record variability in time history analysis of the MWFRS

The first phase of the project aimed to identify the underlying reasons why wind demands estimated through wind time history analysis have been seen on occasion to exceed demand envelopes estimated from equivalent static wind loads (ESWLs). The investigation of this first phase of the project was on studying the variability in wind demands estimated from time history loading due to the inherent record-to-record variability that is captured in traditional wind design using expected peak demands. To investigate the role of record-to-record variability, the time history response of three archetype buildings is first carefully studied in terms of the peak distributions of the demand-to-capacity ratios (DCRs). The record-to-record variability in the dynamic wind loads is modeled through the adoption of a state-of-the-art and wind tunnel-validated stochastic wind load model that is calibrated to building specific wind tunnel data associated with the archetype buildings. The DCR distributions are compared to the ESWL envelopes as well as the point values obtained from the raw wind tunnel data (i.e., the one experimental realization of the loading process). Consistency between the stochastic wind loads and the wind tunnel is ensured by using the same wind tunnel data for calibration of the stochastic wind load model. Secondly, a global sensitivity analysis is carried through leveraging both second-order methods (variance-based approaches) in terms of Sobol indices so as to compare the variability in the DCRs, as well as other response parameters of the archetype buildings, produced by record-to-record variability to that produced by other important and uncertain system parameters (e.g., uncertainties associated with the material parameters and damping of the system).

1.1 Dynamic response framework

1.1.1 Overview

To model the elastic/inelastic dynamic response of the MWFRS of the archetype systems considered in the study, the stress resultant modeling environment outlined in [1.6], and that underpins the WiRA modeling environment, is adopted. The next sections will provide a brief overview of the theory behind this modeling environment.

1.1.2 Mechanical model and elastic solution

Mechanical model

To model plasticity that distributes along beam-column elements in terms of the resultant cross-section forces (bending moments and axial forces) and the related generalized cross-section strains (centroidal axial strain and curvature), a displacement-based formulation is adopted. In this formulation, the displacements, $\mathbf{v}(x) = \{v_x(x), v_y(x), v_z(x)\}^T$, along the element in the local x , y and z coordinate system, with the x -axis coincident with the axis of the member, are related to the 12×1 vector of element end displacements, \mathbf{u} , as:

$$\mathbf{v}(x) = \mathbf{N}(x)\mathbf{u} \quad (1.1)$$

where $\mathbf{N}(x)$ is a 3×12 matrix containing the interpolation functions modeling the variations of displacements along the member. Based on Euler-Bernoulli beam theory, the associated generalized cross-section deformations of the element, $\mathbf{d}(x)$, can be expressed as:

$$\mathbf{d}(x) = \{\epsilon_x(x), \kappa_z(x), \kappa_y(x)\}^T = \left\{ \frac{\partial v_x(x)}{\partial x}, \frac{\partial^2 v_y(x)}{\partial x^2}, -\frac{\partial^2 v_z(x)}{\partial x^2} \right\}^T \quad (1.2)$$

where ϵ_x , κ_z and κ_y are the axial deformation and curvatures in the local x , y , and z directions, which can be expressed in terms of element end displacements as:

$$\mathbf{d}(x) = \mathbf{B}(x)\mathbf{u} \quad (1.3)$$

with $\mathbf{B}(x)$ the generalized strain-deformation matrix whose terms are defined through the first and second derivatives of the displacement interpolation functions. The resultant cross-section forces at each section along the element $\mathbf{D}(x)$, i.e. the axial force $N_x(x)$ and bending moments $M_z(x)$ and $M_y(x)$, are related to the generalized strains through the following constitutive relation:

$$\begin{aligned} \mathbf{D}(x) &= \{N_x(x), M_z(x), M_y(x)\}^T \\ &= \mathbf{k}_s(x)\mathbf{d}(x) \end{aligned} \quad (1.4)$$

where $\mathbf{k}_s(x)$ is the section stiffness matrix. Based on the principle of virtual displacements, the element end forces can be related to the section forces through equilibrium and conveniently solved for through numerical integration as:

$$\mathbf{q} = \int_0^L \mathbf{B}^T(x) \mathbf{D}(x) dx \approx \frac{L}{2} \sum_{i=1}^{N_I} \mathbf{B}^T(x_i) \mathbf{D}(x_i) w_i \quad (1.5)$$

where L is the length of the element, N_I is the number of integration points along the element, w_i is the weight associated with the i th integration point while x_i is the location of the i th integration point. Substituting $\mathbf{d}(x)$ into Eq. (1.5) and linearizing with respect to the element end displacements gives the element stiffness matrix \mathbf{k} :

$$\mathbf{k} = \frac{\partial \mathbf{q}}{\partial \mathbf{u}} \approx \frac{L}{2} \sum_{i=1}^{N_I} \mathbf{B}^T(x_i) \mathbf{k}_s(x_i) \mathbf{B}(x_i) w_i \quad (1.6)$$

Elastic solution

Given the stress-resultant/generalized strain model described above, the elastic dynamic solution of a structural system subject to general stochastic excitation, $\mathbf{F}(t)$, can be estimated by solving the following dynamic equilibrium equation:

$$\mathbf{M}\ddot{\mathbf{X}}(t) + \mathbf{C}\dot{\mathbf{X}}(t) + \mathbf{K}\mathbf{X}(t) = \mathbf{F}(t) \quad (1.7)$$

where $\mathbf{X}(t)$, $\dot{\mathbf{X}}(t)$ and $\ddot{\mathbf{X}}(t)$ are the displacement, velocity and acceleration response vectors in global coordinates while \mathbf{M} , \mathbf{C} and \mathbf{K} are the mass, damping and elastic stiffness matrices of the system. In particular, the stiffness matrix \mathbf{K} is determined through assembly of element stiffness matrices, defined through Eq. (1.6), after discretization of the structural system into N_e beam-column elements. Due to the linearity of the system, Eq. (1.7) can be efficiently solved through direct modal integration [1.20], and therefore through solving the following system of uncoupled equations:

$$\ddot{\bar{X}}_{\phi_k}(t) + 2\xi_k \omega_k \dot{\bar{X}}_{\phi_k}(t) + \omega_k^2 \bar{X}_{\phi_k}(t) = \frac{\phi_k^T \mathbf{F}(t)}{m_k} \quad k = 1, \dots, m \quad (1.8)$$

where ω_k , m_k , ξ_k and ϕ_k are the k th circular frequency, modal mass, damping ratio and mode shape vector; while $\bar{X}_{\phi_k}(t)$, $\dot{\bar{X}}_{\phi_k}(t)$ and $\ddot{\bar{X}}_{\phi_k}(t)$ are the k th modal displacement, velocity, and acceleration responses. The displacement response at the ends of each element in global coordinates, $\mathbf{U}_j(t)$ for $j = 1, \dots, N_e$, can then be extracted from $\mathbf{X}(t)$. The corresponding stress-resultants at the i th integration point of the j th element, $\mathbf{D}_j(x_i, t)$, can then be determined using Eqs. (1.3) and (1.4), as:

$$\mathbf{D}_j(x_i; t) = \mathbf{k}_{s_j}(x_i) \mathbf{B}_j(x_i) \mathbf{T}_j \mathbf{U}_j(t) \quad (1.9)$$

with \mathbf{T}_j the global to local coordinate transformation matrix of the j th element.

Yield domains and the demand to capacity ratios (DCRs)

Given a structural system discretized into N_e beam-column elements, yielding will not occur if the following holds for each integration point of the discretization:

$$\mathbf{N}_{ji}^T \mathbf{D}_{s_j}^E(x_i; t) - \mathbf{R}_j(x_i) \leq \mathbf{0} \quad \text{for } i = 1, \dots, N_{I_j} \quad \text{and } j = 1, \dots, N_e \quad (1.10)$$

where $\mathbf{R}_j(x_i)$ is the plastic resistance vector defined from the linearization of the stress-resultant yield domains associated with each integration point of the discretization; \mathbf{N}_{ji} is the block diagonal matrix collecting the unit external normals associated with each surface of the linearized yield domain; while $\mathbf{D}_{s_j}^E(x_i; t)$ is the elastic dynamic response at the i th integration point of the j th element.

Given a linearization with $k = 1, \dots, N_k$ surfaces, it follows that the demand to capacity ratio for the k th surface of integration point x_i , DCR_{ik} , can be estimated as the maximum over time of the demand (i.e., the maximum of $\mathbf{D}_{s_j}^E(x_i; t)$ over t) projected in the direction of the k th surface, $\hat{D}_{s_{jk}}^E(x_i)$, and divided by the magnitude of the resistance vector associated with the k th surface, R_{jik} , i.e., $\text{DCR}_{ik} = \hat{D}_{s_{jk}}^E(x_i)/R_{jik}$. It follows that the maximum demand-to-capacity ratio at the i th integration point of the j th element can then be defined as the maximum demand-to-capacity ratio over all surfaces of the linearization, i.e., as:

$$\text{DCR}_{ji} = \max_{k=1, \dots, N_k} \left[\frac{\hat{D}_{s_{jk}}^E(x_i)}{R_{jik}} \right] \quad \text{for } i = 1, \dots, N_{I_j} \quad \text{and } j = 1, \dots, N_e \quad (1.11)$$

1.1.3 Stochastic wind load model

To characterize the external wind loads, wind tunnel test data were considered. These consisted of the simultaneous measurement of pressures at a number of taps located on the surface of a rigid scale model of the building. Through integration to the geometric centers of each floor of the building model, these pressures can be used to estimate an experimental realization of the vector collecting the external dynamic wind loads, indicated in the following as $\mathbf{F}(t)$. Time/frequency scaling of $\mathbf{F}(t)$ can then be achieved through imposing similitude between the Strouhal number at model and full scale.

Under the common assumption of stationarity and ergodicity of the vector-valued stochastic process $\mathbf{F}(t)$, the wind tunnel realization of $\mathbf{F}(t)$ can be used to calibrate an appropriate non-Gaussian stochastic simulation model. To this end, a translation model is considered in this work. The model is based on first approximating $\mathbf{F}(t)$ through a Gaussian process, $\mathbf{F}^{\mathcal{GP}}(t)$, whose second-order properties match those of the original process, and, secondly, using $\mathbf{F}^{\mathcal{GP}}(t)$ as input to a translation process whose marginal distributions match those of the non-Gaussian process $\mathbf{F}(t)$.

To simulate random realizations of $\mathbf{F}^{\mathcal{GP}}(t)$, a proper orthogonal decomposition (POD) based spectral representation model is adopted [1.5, 1.17, 1.15, 1.22, 1.16,

1.9]. In particular, to estimate the frequency dependent eigenvalues and eigenvectors of $\mathbf{F}(t)$, the following spectral eigenvalue problem can be solved:

$$[\mathbf{S}_{\mathbf{F}}(\omega; \alpha) - \Lambda_i(\omega; \alpha)\mathbf{I}]\Psi_i(\omega; \alpha) = 0 \quad (1.12)$$

where ω is the circular frequency, \mathbf{I} is the identity matrix, $\mathbf{S}_{\mathbf{F}}$ is the double-sided cross power spectral density matrix estimated from the wind tunnel realization of $\mathbf{F}(t)$, while Λ_i and Ψ_i are the i th frequency dependent eigenvalue and eigenvector of $\mathbf{F}(t)$. The knowledge of Λ_i and Ψ_i can be used to give $\mathbf{F}^{\mathcal{GP}}(t)$ the following truncated representation of order N_m :

$$\mathbf{F}^{\mathcal{GP}}(t) \approx \tilde{\mathbf{F}}^{\mathcal{GP}}(t) = \bar{\mathbf{F}} + \sum_{i=1}^{N_m} \tilde{\mathbf{F}}^{(i)}(t) \quad (1.13)$$

where $\bar{\mathbf{F}}$ is the mean wind loads (estimated directly from the wind tunnel data), while $\tilde{\mathbf{F}}^{(i)}(t)$ are N_m zero mean independent subprocesses which can be given the following spectral representation:

$$\tilde{\mathbf{F}}^{(i)}(t) = \sum_{j=0}^{N_\omega-1} 2|\Psi_i(\omega_j)|\sqrt{\Lambda_i(\omega_j)\Delta\omega} \cos(\omega_j t + \boldsymbol{\vartheta}_j(\omega_j) + \theta_{ij}) \quad (1.14)$$

where: $\Delta\omega$ is the frequency increment with $\omega_j = j\Delta\omega$; N_ω is the total number of discrete frequencies, therefore, leading to a Nyquist (cutoff) frequency of $N_\omega\Delta\omega/2$; θ_{ij} is an independent random variable characterizing the stochastic nature of the wind loads and uniformly distributed over $[0, 2\pi]$; while $\boldsymbol{\vartheta}_j(\omega_j) = \tan^{-1}(\text{Im}(\Psi_i(\omega_j))/\text{Re}(\Psi_i(\omega_j)))$.

To capture the non-Gaussian nature of $\mathbf{F}(t)$, the Gaussian process $\tilde{\mathbf{F}}(t)$ can be used as input to a translation model [1.11, 1.13]. Under this assumption, the n th component of $\mathbf{F}(t)$ is given by:

$$F^{(n)}(t; \alpha) = F_{F^{(n)}}^{-1} \left\{ \Phi \left[\frac{\tilde{F}^{\mathcal{GP}(n)}(t; \alpha) - \mu_{F^{(n)}}(\alpha)}{\sigma_{F^{(n)}}(\alpha)} \right] \right\} \quad (1.15)$$

where Φ is the standard normal distribution function, $\mu_{F^{(n)}}$ and $\sigma_{F^{(n)}}$ are the mean and standard deviation of $F^{(n)}(t)$ while $F_{F^{(n)}}$ is the corresponding non-Gaussian marginal distribution. To estimate $F_{F^{(n)}}$, the wind tunnel data can be used to calibrate a kernel-Pareto mixture model [1.24]. In this approach, the possible values that can be assumed by $F^{(n)}$ are divided into the following mutually exclusive regions: 1) a lower tail region, defined as $F^{(n)} \leq v_l$ with v_l the lower tail threshold; 2) a central region, defined as $v_l < F^{(n)} < v_u$ with v_u the upper tail threshold; and 3) an upper tail region, defined as $F^{(n)} \geq v_u$. By recognizing that the majority of the experimental data will be in the central region, the marginal distribution function is fitted here using kernel density. By then observing how the tail regions are

populated by extreme values, the marginal distribution functions of these regions are assumed to follow an extreme Pareto distribution. Within this context, the following mixture model can be defined for the pdf of $F^{(n)}$:

$$f_{F^{(n)}}(F^{(n)}) = 1_{\{F^{(n)} \leq v_l\}} f_{P,l}(F^{(n)}) + 1_{\{v_l < F^{(n)} < v_u\}} f_{kde}(F^{(n)}) + 1_{\{F^{(n)} \geq v_u\}} f_{P,u}(F^{(n)}) \quad (1.16)$$

where $1_{\{*\}}$ is the indicator function, $f_{P,l}$ and $f_{P,u}$ are the Pareto fitted pdfs at the lower and upper tails, while f_{kde} is the estimated kernel density in the middle region. As outlined in [1.24], this model not only is well suited for capturing the generally non-Gaussian features seen in wind loads, but can also be calibrated (including the identification of the bounds v_l and v_u) in a semi-automated fashion directly from classic wind tunnel data.

The representation of $\mathbf{F}(t)$ defined by Eqs. (1.13) to (1.16) is convenient from a simulation standpoint as: 1) the subprocesses of Eq. (1.14) are independent and can therefore be simulated individually using efficient algorithms based on the Fast Fourier Transform [1.8]; and 2) only the first few subprocesses are generally required for accurately representing $\mathbf{F}(t)$.

1.1.4 The archetype buildings

Archetype buildings with steel and reinforced concrete main wind force resisting systems (MWFRS) were considered in the study of the importance of record-to-record variability. The MWFRS of each archetype was based on those developed by the performance-based (PBD) Task Committee of the ASCE 7-22 Wind Loads Subcommittee. The archetype buildings were developed with the end goal of furthering the advancement of performance-based wind design (PBWD). The building geometries, as well as their structural systems, are summarized in Fig. 1.1.

Wind tunnel tests for all three building shapes were conducted by CPP Wind Engineering & Air Quality Consultants (one of the project sponsors). For the 180 m rectangular building, wind tunnel tests were carried out for roughness associated with Exposures B and C of ASCE 7 standard [1.1]. These exposures respectively represent areas with abundant and closely scattered obstacles (Exposure B) and areas with more loosely scattered obstructions (Exposure C), with Exposure B mimicking a Urban and suburban areas, wooded areas, or other terrain with numerous closely spaced obstructions.

The test data was associated with relevant climatological information therefore resulting in ESWLs being defined for the wind climates of New York (NY) and Miami. These loads were then utilized to create five unique steel and reinforced concrete designs. These designs conform to steel and reinforced concrete LRFD requirements with load combinations derived from the ASCE 7-22 standard.

Of the five buildings indicated in Fig. 1.1, an extensive quality assurance/quality control (QA/QC) of the designs and associated WiRA finite elements models of this project was conducted. This revealed the following shortcomings:

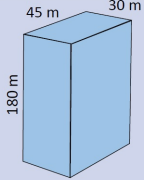
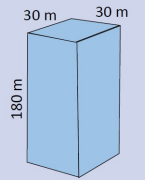
	Building shape			
	45 m x 30 m		30 m x 30 m	
				
Wind climate (Exposure)	NY (C)	Miami (B)	NY (C)	Miami (C)
Steel megabraces	x	x	x	
Concrete core	x			
Concrete core with fin walls	x			

Figure 1.1: Archetype buildings.

1. The square NY steel design did not meet the DCR targets;
2. The rectangular NY steel building did not use building-specific ESWs during design (approximate ESWs were used based on those defined for the square NY steel archetype);
3. The finite element model of the designers associated with the concrete core with fin walls could not be located by the designers;
4. The ESWs used in the design of the rectangular Miami steel building were based on preliminary natural frequencies that were significantly different from the natural frequencies of the final designed building.

These shortcomings resulted in the redesign of the square NY steel archetype so has to meet the design criteria (all DCRs less than unity for LRFD based on a 700-year wind load (Risk Category II)). In addition, the following caveats must be noted: 1) all Phase 2 reliability results of the rectangular NY steel building and rectangular Miami steel building cannot be considered representative of the reliability obtained by buildings conforming to current practices as the provided archetypes require redesign in light of the discoveries of the QA/QC of this project. They are therefore not included in this report. In addition, because the original finite element model of the concrete core with fin wall design could not be provided to the project team therefore preventing a QA/QC, it was dropped in all subsequent analyses. Details on the QA/QC of the WiRA models of this project for the NY square steel archetype and the NY rectangular concrete core archetype are reported in Appendix A.

For phase 1, the square NY steel design, the rectangular Miami steel building, and the concrete core NY building were considered as they cover both steel and reinforced concrete systems as well as exposures B and C.

1.2 Uncertainty in the DCRs generated by record-to-record variability

1.2.1 Load case

For the estimation of the DCRs, the analyses were carried out for α varying from $\alpha = 0^\circ$ to $\alpha = 350^\circ$ in 10-degree increments with all parameters of the structural system set to expected values. For each wind direction, 100 random wind records were considered, i.e., 100 realizations of the stochastic wind load model of Sec. 1.1.3 that was calibrated to the wind tunnel time history data provided by CPP. The stochastic wind load records were combined with the gravity loads following the load combination suggested in the ASCE Prestandard on PBWD v1.1 and therefore following the combination:

$$1.0DL + 1.0LL_r + 1.0W \tag{1.17}$$

where LL_r is the reduced live load, DL is the dead load (including superimposed dead load), while W are the wind loads which in the following will be either the 700-year ESWLs provided by CPP for design or the 700-year wind time history loading corresponding to either the stochastic realizations or the scaled wind tunnel realization. All dead load values followed those provided by the designers of the archetypes. It should be noted that when W is an ESWL, all ESWL distributions provided by CPP are considered.

1.2.2 Results

Comparison between DCRs from ESWLs and dynamic wind loads

DCRs were estimated for both the ESWLs as well as the wind tunnel realization of the dynamic wind loads. The comparison in the DCRs (see Sec. 1.1.2 for background on how the DCRs are calculated for general 3D yield domains) is shown in Fig. 1.3 for the NY square steel archetype. As can be seen, the correspondence is reasonable and in line with exceptions. Figure 1.2 provides a comparison in terms of the following ratio:

$$\frac{DCR_{\max_{WTTH}}}{DCR_{\max_{ESWL}}} \tag{1.18}$$

where $DCR_{\max_{ESWL}}$ and $DCR_{\max_{WT}}$ are the maximum DCR of each element due to the application of ESWLs or dynamic wind tunnel time history (WTTH) loads, respectively. As can be seen, differences can be seen for DCRs estimated from ESWLs as compared to those estimated from the dynamic wind loads. It is interesting to observe how over/underestimation of the DCRs from the use of ESWLs is correlated in space. At first glance, the variability of the ratios of Eq. (1.18) may seem concerning. However, the following observations must be made: 1) the DCRs estimated using ESWLs are based on a probabilistic description of the peak demands

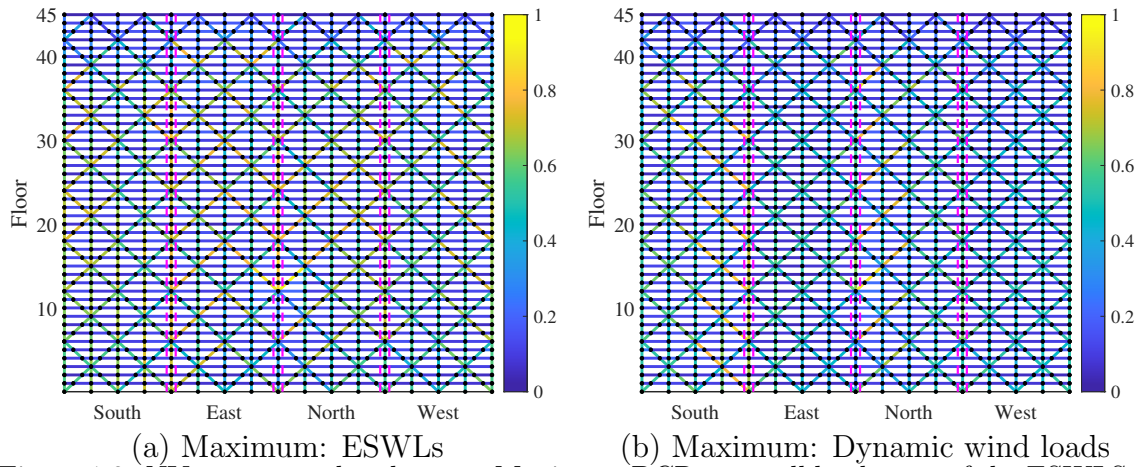


Figure 1.2: NY square steel archetype: Maximum DCRs over all load cases of the ESWLS and over all wind directions for the dynamic wind loads.

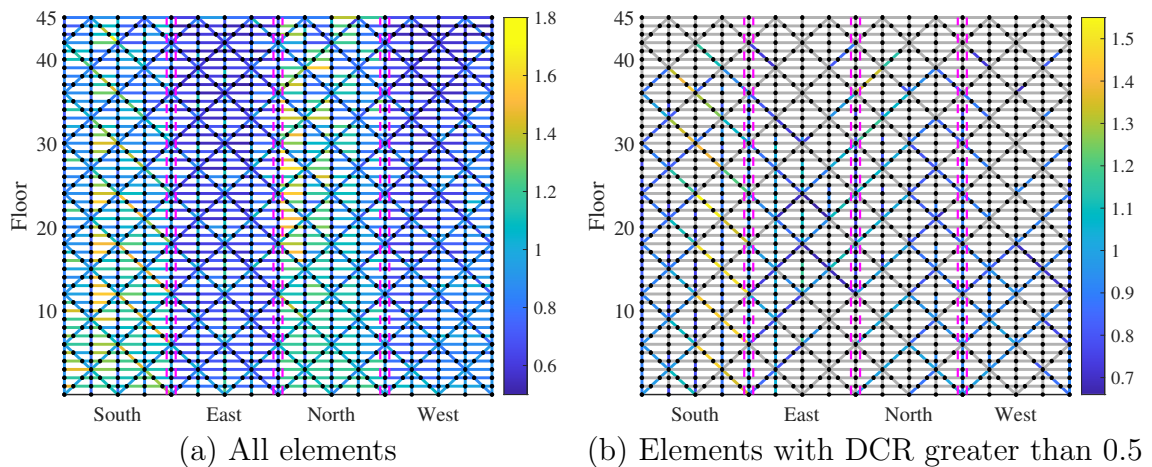


Figure 1.3: NY square steel archetype: Maximum of Eq. (1.18) over all elements.

(expected peak) while the DCRs estimated from the dynamic winds loads are based on the peak of a single realization of wind loads; and 2) the ratios are sensitive to the absolute value of the DCRs being compared, i.e., for smaller values of the DCRs, the ratio will increase for the same difference in the DCRs, as illustrated in Fig. 1.2(b) where results are plotted only for components with DCR greater than 0.5 under the dynamic wind loads. In light of these observations, the main takeaway from Fig. 1.2 should be that probabilistic treatment of the peak demands estimated from the use of dynamic wind loads is necessary. As illustrated in Figs. 1.4-1.7, similar results are observed for the Miami rectangular steel archetype as well as the NY rectangular concrete core archetype.

In particular, the greater discrepancies seen for the Miami rectangular steel archetype can be traced back to how, as mentioned in Sec. 1.1.4 the preliminary

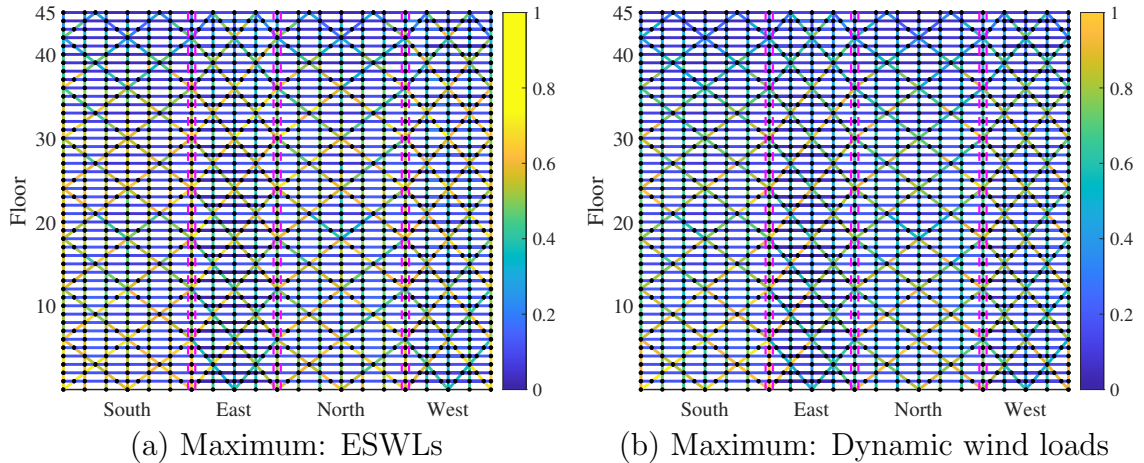


Figure 1.4: Miami rectangular steel archetype: Maximum DCRs over all load cases of the ESWLS and over all wind directions for the dynamic wind loads.

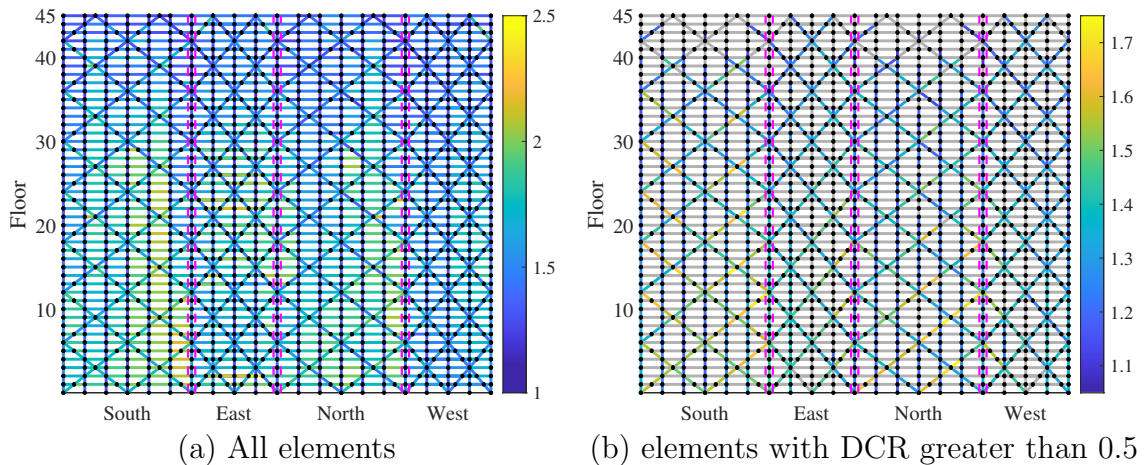
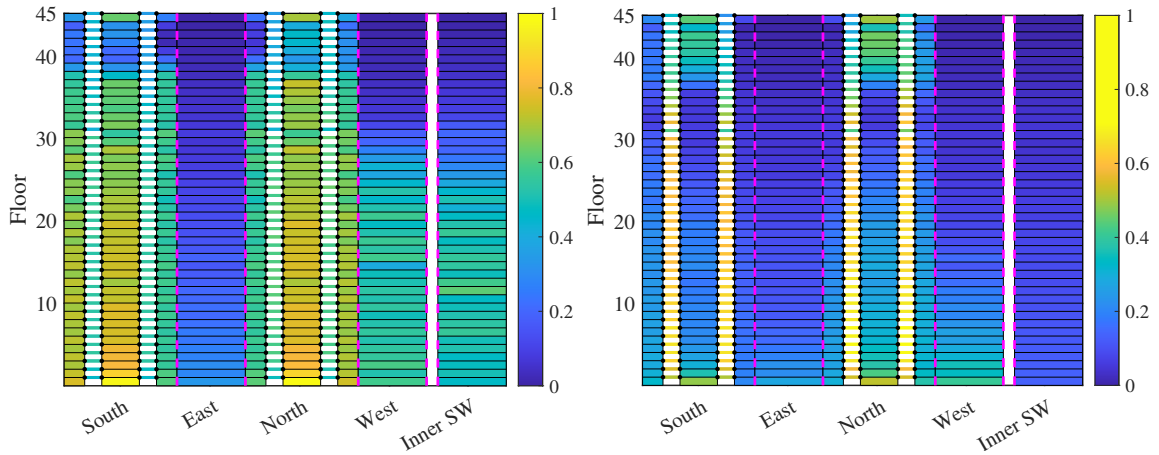
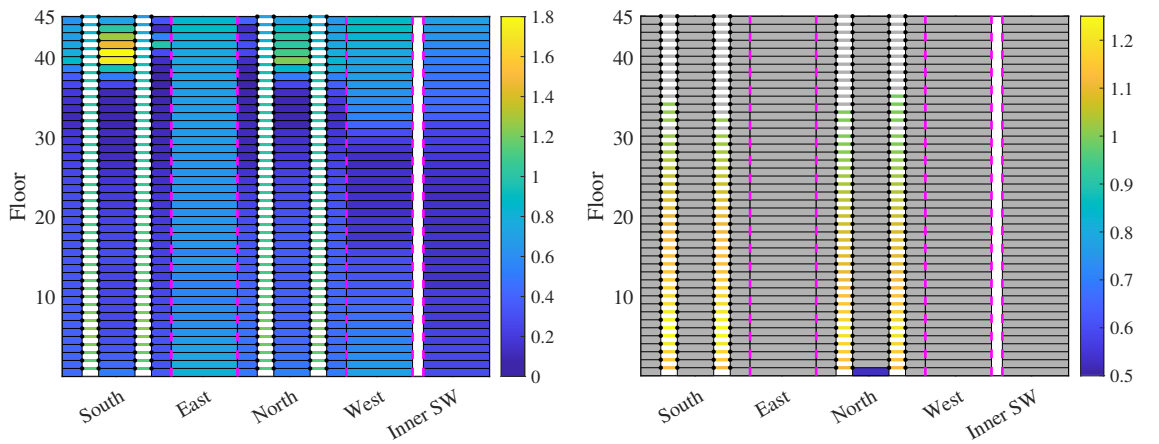


Figure 1.5: Miami rectangular steel archetype: Maximum of Eq. (1.18) over all elements (Note: the ratios of this figure should be interpreted with caution as the preliminary dynamic properties used by CPP to estimate the ESWLS differ significantly from those of the final design therefore indicating that the ESWLS would require updating before the results can be deemed representative).



(a) Maximum: ESWLs (b) Maximum: Dynamic wind loads
 Figure 1.6: NY rectangular concrete core archetype: Maximum DCRs over all load cases of the ESWLs and over all wind directions for the dynamic wind loads.



(a) All elements (b) Elements with DCR greater than 0.5
 Figure 1.7: NY square steel archetype: Maximum of Eq. (1.18) over all elements.

dynamic properties used by CPP to estimate the ESWLs differ significantly from those of the final design therefore indicating that the ESWLs would require updating. Indeed, the ESWLs were estimated based on fundamental frequencies of 0.4502 Hz, 0.3587 Hz, and 0.9891 Hz while the fundamental frequencies of the MWFRS designed using the ESWLs resulted to be 0.2523 Hz, 0.2919 Hz, and 0.6007 Hz.

Record-to-record variability and the DCRs

Before discussing the results of this section, it should be noted that in all comparison of ESWLs responses with raw time history peaks (whether derived from the wind tunnel record or a realization of the calibrated stochastic wind load model), that these data are not considered in the development of the ESWLs. The expected peak response, used in developing the ESWLs, is generally based on Davenport's peak factor approach [1.7], which uses the the statistics of the overall signal for estimation of the distribution of extremes. While raw peaks could obviously be extracted from the record, and treated with the generalized least square method or similar, they should not in general be used in a raw manner. The purpose of the following discussions is to quantify the variability in the peaks when using wind time history analysis in light of how such approaches are often carried out using a single wind record for each wind direction. The next steps would be to suggest appropriate methods to use in wind time history analysis that treat peaks using statistical methods.

Figure 1.8 reports the variability in the maximum DCR over all components for 100 realizations of the stochastic wind load model of Section 1.1.3 for the NY square steel archetype. This enables the illustration of the effects of record-to-record variability and how this variability compares to the ESWL envelope as well as the DCRs estimated from the wind tunnel realization of the dynamic wind loads. The following observations can be made from Fig. 1.8:

1. Significant variability in the maximum DCR can be generated from record-to-record variability;
2. Although not a direct objective in the development of ESWLs, it is interesting to observe how the ESWL load cases generally enveloped the DCRs estimated from the wind tunnel record as well as the DCRs generated from the realization of the stochastic wind loads, but this cannot be guaranteed as clearly seen for the NY square steel archetype and a wind direction of 270° (see Fig. 1.8);
3. There would seem to be evidence that the peak DCR estimated from the wind tunnel realization of the dynamic wind loads has a positive bias, i.e., they would seem on average to be larger) as compared to the DCRs generated from the stochastic wind loads (i.e., the DCRs from the single wind tunnel record tend to be larger than the expected value of the DCRs estimated from the stochastic wind load realizations). Although the underlying reasons for

this discrepancy is beyond the scope of this project, it is believed to be related to the difficulty in capturing the true nature of the parent distributions in the translation model capturing the non-Gaussian features of the excitation.

The observation of the second point is of fundamental interest this this project. Indeed, from Fig. 1.8 and wind direction 270° , it is clearly evident that the treatment of the record-to-record variability through the expected peak value can lead to DCRs that exit the DCR envelope generated by the application of the ESWLs. In other words, wind demands estimated through wind time history analysis can easily exceed those estimated using ESWLs that are based on expected peak wind demands. This discrepancy implies the need for statistical methods for treating the peaks that are estimated from wind time history analysis if consistency is to be achieved with current state-of-the-art wind analysis methods. A single wind record may well exceed the expected peak wind demand (or, on the contrary, underestimate the expected wind demand). This is further illustrated in Fig. 1.9 that reports the time history responses of the critical DCR projection (indicated as DCR_{pc}) for the component with maximum DCR estimated from the application of the ESWLs. As can be seen, the mean peak DCR estimated from the 100 realizations of the stochastic excitation is well below the ESWL envelope. However, if the largest peak DCR is considered from the 100 realizations, then the ESWL envelope is exceeded. It is important to observe this is not a direct comparison as the peaks of the ESWL approach are expected values while the largest peak over 100 realizations of the stochastic wind load model is a realization of the largest value to occur when selecting from 100 independent and identically distributed peaks. Notwithstanding this, it provides an effective illustration of the variability of the peaks and how this compares to the expected value, especially in light of how many wind time history analysis approaches are being implemented using a single wind tunnel record for each critical wind direction. In particular, from the zoom of Fig. 1.10, it can be seen that the exceedance of the ESWL envelope is due to the largest peak of a cluster occurring with a frequency close to the fundamental vibration mode of the MWFRS. To account for this phenomenon, wind time history analysis should consider a suite of records for each wind direction therefore enabling the direct evaluation of the expected wind demands as well as the variation from this value due to record-to-record variability.

The third point would suggest that the real wind load process (defined here as the wind load process observed in the wind tunnel) cannot be modeled as a non-Gaussian stationary stochastic process, as is the conventional thinking underlying the probabilistic analysis of wind load effects in the time or frequency domain as well as the stochastic wind load model of Sec. 1.1.3. Rather, there would seem to be preliminary evidence that a more complex process may exist producing larger peaks than seen for a single non-Gaussian stationary stochastic process (note that the stochastic wind load model of Sec. 1.1.3 was calibrated using 25 POD modes, as suggested in [1.9], and was seen to reproduce the second-order properties of the wind

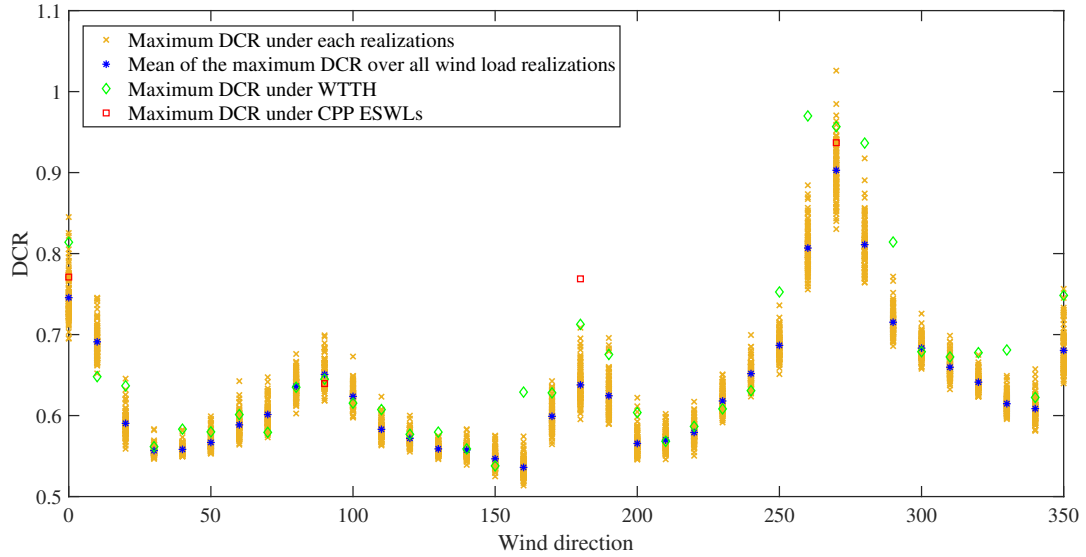


Figure 1.8: NY square steel archetype: record-to-record variability for all wind directions and the maximum DCR over all components.

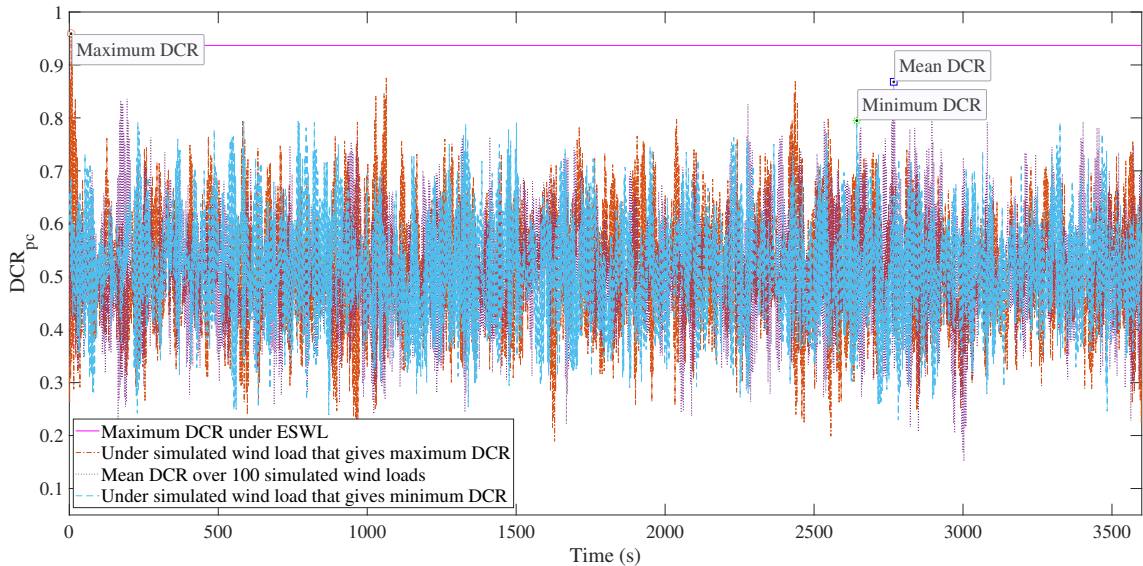


Figure 1.9: NY square steel archetype: Time history of the critical DCR projection for the component with maximum DCR estimated from the ESWLs.

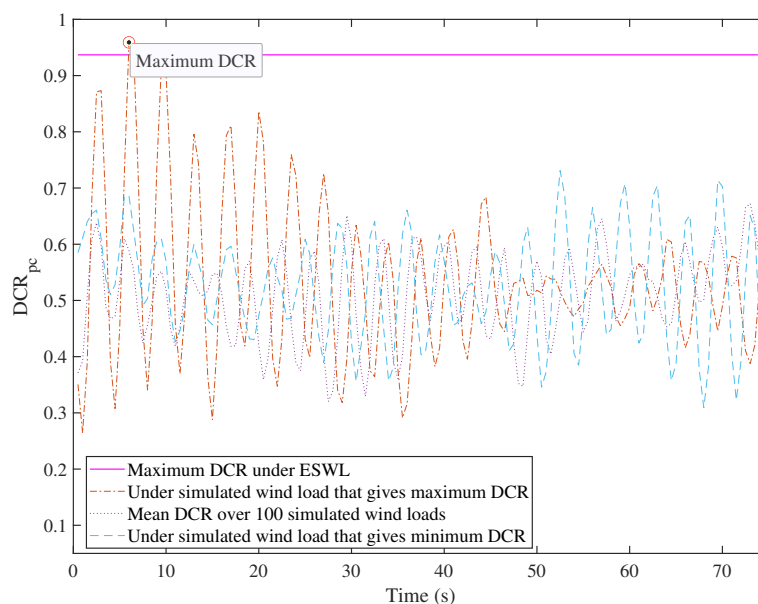


Figure 1.10: NY square steel archetype: zoom of the time history of Fig. 1.9 around the maximum DCR (Note: The applied wind loads were linearly ramped using the model outlined in Chapter 2, Eq. (2.6)).

load process with high accuracy as well as the non-Gaussian features of the floor loads). The lack of repeated realization of the wind load process in the wind tunnel (i.e. only one wind tunnel load realization for each wind direction was available) did not allow the further investigation of this point.

Figures 1.11 and 1.12 report the results for the Miami rectangular steel archetype and NY rectangular concrete core archetype. Similar results can be observed as seen for the NY square steel archetype. It is interesting to observe that there would be evidence from Fig. 1.11 that the variability in the maximum DCR over all components is larger than that seen for the other archetypes. This would suggest that record-to-record may be sensitive to surrounds (the Miami rectangular steel archetype is the only archetype of this project that has a wind exposure corresponding to B). In addition, for the Miami rectangular steel archetype, the tendency for the peak DCRs obtained from the application of the wind tunnel dynamic wind loads to exceed those estimated from the application of the stochastic wind load model of Section 1.1.3 would seem to be markedly more evident than for the NY square steel archetype. This once again suggests there may be an inherent limitation to modeling dynamic wind loads as non-Gaussian stationary stochastic processes. While this goes beyond the scope of this project, some further discussion on the calibration of the stochastic wind load model of Section 1.1.3 to the Miami rectangular steel archetype is presented in Appendix B in order to provide confidence that the differences seen in this section are not due to a calibration error in the model.

To further characterize the effects of record-to-record variability on the peak

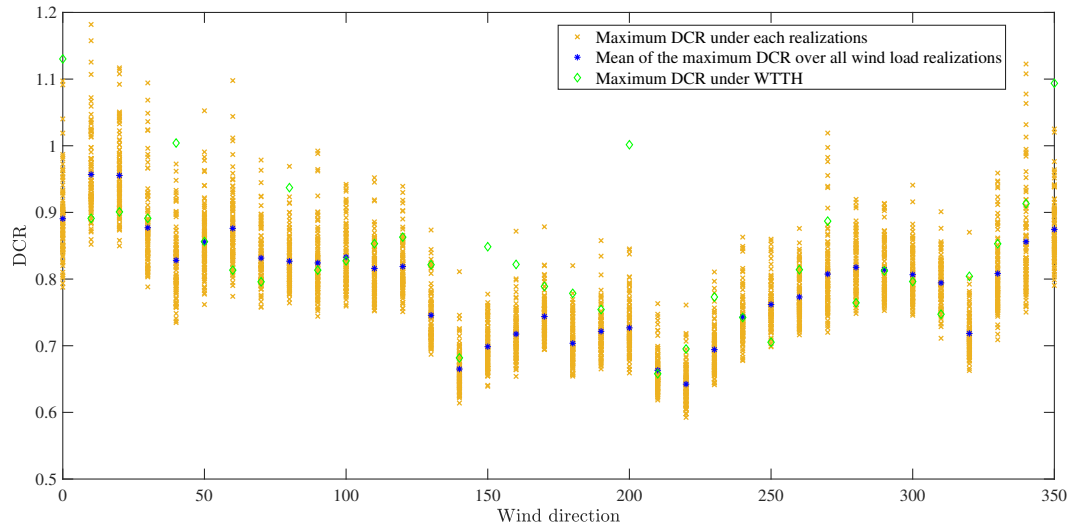


Figure 1.11: Miami rectangular steel archetype: record-to-record variability for all wind directions and the maximum DCR over all components (Note: the responses estimated from the application of the ESWLs are not reported as the preliminary dynamic properties used by CPP to estimate the ESWLs differ significantly from those of the final design therefore indicating that the ESWLs would require updating before the results can be deemed representative).

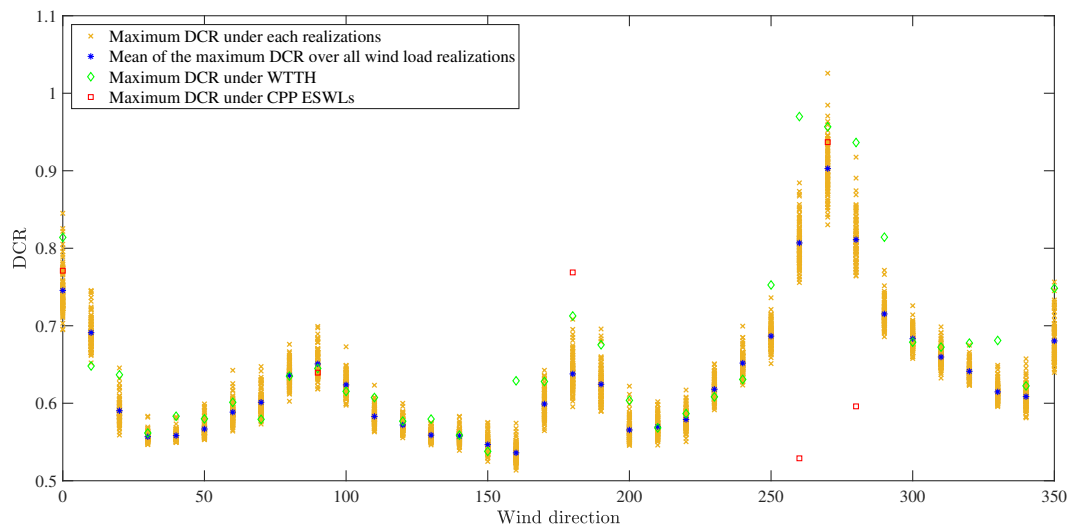
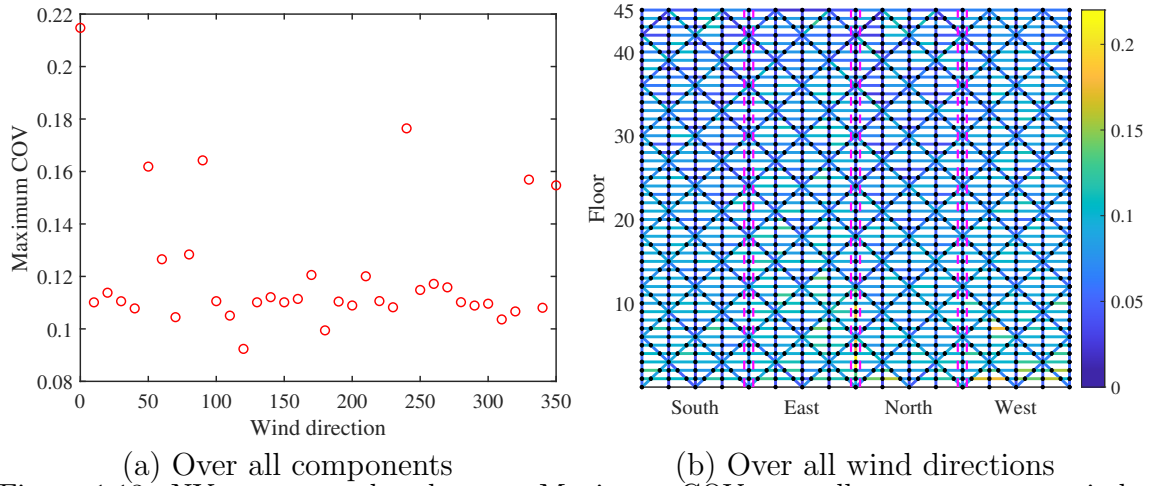


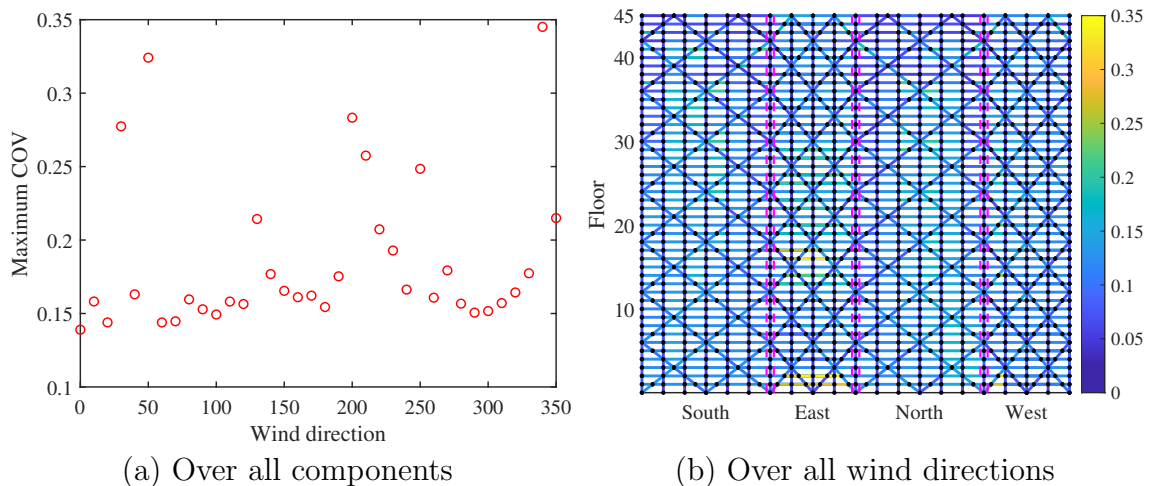
Figure 1.12: NY rectangular concrete core archetype: record-to-record variability for all wind directions and the maximum DCR over all components.

DCRs, Figs. 1.13-1.15 reported the coefficients of variation (COV) of the peak DCRs due to record-to-record variability for the three archetype systems considered in terms of the maximum over all components for each wind direction as well as the maximum for each component over all wind directions. As can be seen, the COVs can reach values of 0.8 with the range 0.1 to 0.2 most typical. In addition, it is interesting to observe the spatial correlation that exists in the maximum COVs between the components. This is seen for all three archetype systems suggesting this is a phenomenon that is not unique to a particular system or wind climate. It is interesting to observe from Fig. 1.14 how the COVs are generally larger for the Miami rectangular steel archetype, as compared to the NY square steel archetype, suggesting that more complex surroundings may increase the variability of the DCRs due to record-to-record variability. The occurrence of relatively high values of COVs for the NY rectangular concrete core archetype as compared to the steel systems can be traced back to how many components of this system had low wind demands leading to artificially large COVs. To partially mitigate this, Fig. 1.15 only reports the COVs for components with expected peak DCRs greater than 0.1.

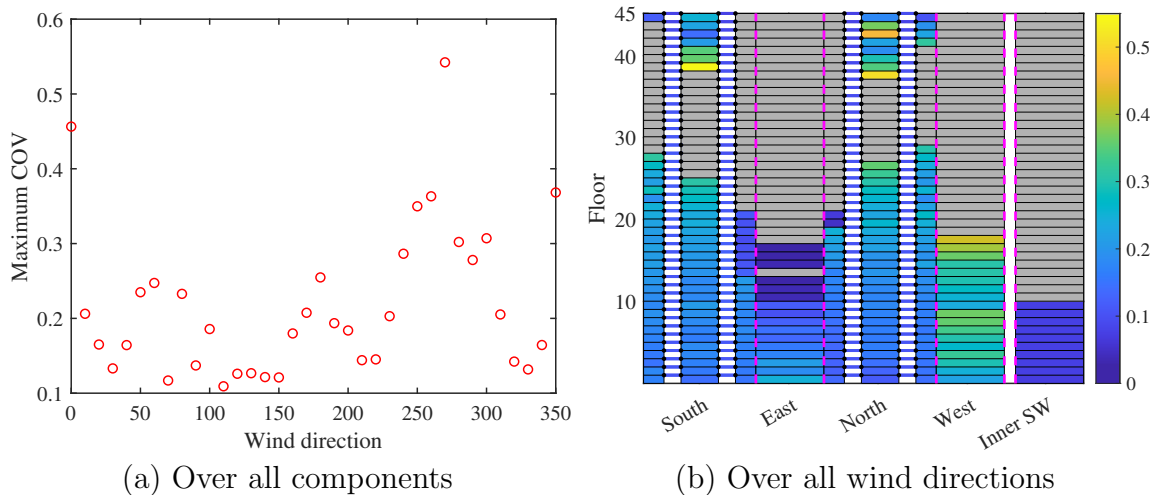
Figure 1.16 reports the histograms of the peak DCRs for the six components with the largest DCRs of the NY square steel archetype. The location of the components is illustrated in Fig. 1.17. As can be seen, the histograms tend to be skewed towards larger values, as would be expected (i.e., by definition, DCRs are bounded from below by zero). Similar results were observed for the Miami rectangular steel archetype and NY rectangular concrete core archetype. Overall, this result indicates how the variability in the DCRs generated by record-to-record variability will generally be skewed towards peaks that exceed the expected peak value that is at the core of current design practice. In summary, methods need to be introduced that enable a probabilistic treatment of the peaks observed in wind time history analysis. Because of the interest in nonlinear analysis when applying PBWD, these methods cannot be based on traditional assumptions of elastic responses and is an important avenue of future research for the consistent application of PBWD.



(a) Over all components (b) Over all wind directions
 Figure 1.13: NY square steel archetype: Maximum COV over all components or wind direction.



(a) Over all components (b) Over all wind directions
 Figure 1.14: Miami rectangular steel archetype: Maximum COV over all components or wind direction.



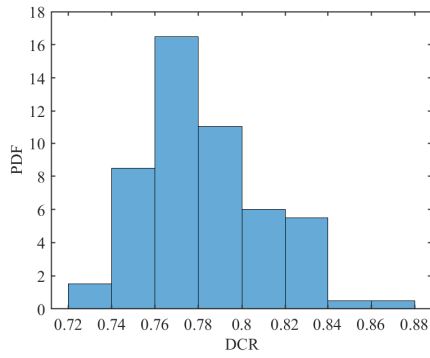
(a) Over all components (b) Over all wind directions
 Figure 1.15: NY rectangular concrete core archetype: Maximum COV over all components or wind direction (components with mean DCR less than 0.1 indicated in gray).

1.3 Sensitivity analysis

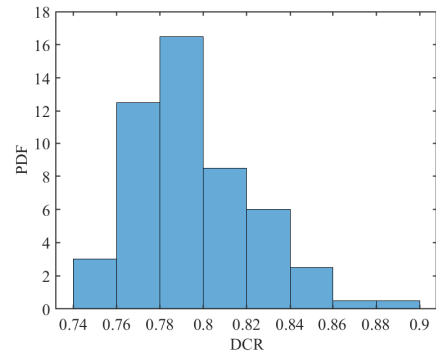
1.3.1 Sobol indices

To investigate the relative importance of record-to-record variability as compared to other system uncertainties, a formal sensitivity analysis was carried out based on the variance methods suggested by Sobol [1.19]. Variance-based sensitivity analysis represents a global sensitivity analysis approach within a probabilistic framework. It involves partitioning the output variance of a model or system into portions assigned to inputs or groups of inputs. For instance, in a two-input, one-output model, 70% of output variance might result from variance in the first input, 20% from the second, and 10% due to their interaction. These percentages illustrate sensitivity measures. Variance-based sensitivity techniques have advantages as they examine sensitivity across the entire input space (making it a global method), can manage nonlinear outputs, and are capable of evaluating the impact of interactions in non-additive systems.

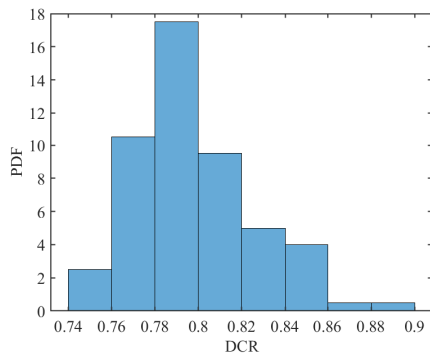
The “first-order sensitivity index”, also known as the “main effect index”, represents a direct variance-based sensitivity measure. It quantifies the impact of the variability of a single random input (or group of inputs) averaged over variations in all other input parameters. It is standardized with the total variance, thereby supplying a fractional contribution. The “total-effect index” measures the contribution to the output variance of a given random input, including all variance caused by its interactions, of any order, with any other input variable (or group of input variables). The total-effect indexes were estimated to characterize the relative importance of record-to-record variability as compared to other system uncertainties.



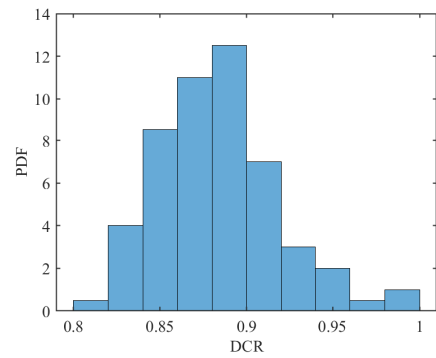
(a) Element 1138



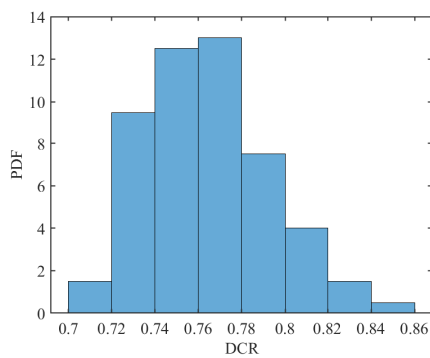
(b) Element 1139



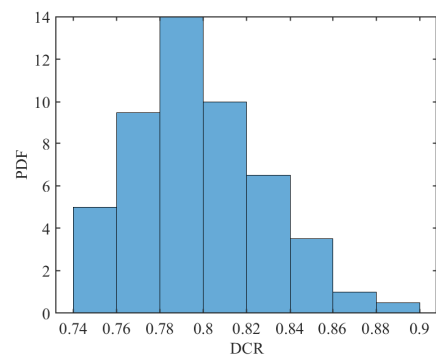
(c) Element 1140



(d) Element 1236



(e) Element 1385



(f) Element 1286

Figure 1.16: NY square steel archetype: histograms of DCRs for key components.

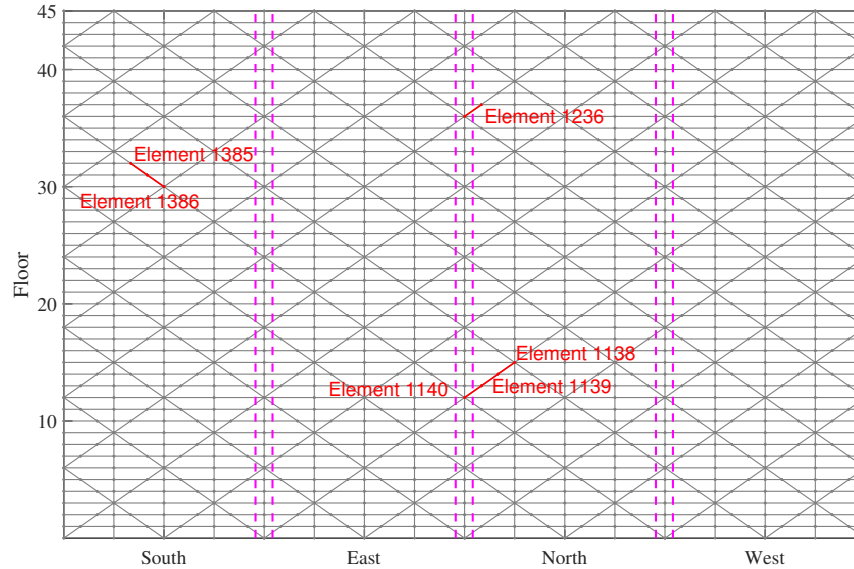


Figure 1.17: NY square steel archetype: location of key components.

1.3.2 Uncertainties and macro parameters

Gravity load and model parameters uncertainties

System and gravity load uncertainties considered are consistent with those used in developing codes and standards. In full reliability analysis, these are to be considered together with the wind hazard uncertainties (i.e., wind speed and direction uncertainties). The dead loads, D , and “arbitrary point-in time” live loads, L_{apt} , are assumed to follow the characteristics summarized in Table 1.3 with w_1 , w_2 , and w_3 random variables modeling the uncertainty that exists when estimating dynamic wind loads from wind tunnel data. Table 1.2 summarizes the statistical information for the basic random variables considered in steel MWFRS with F_y the yield stress, E_s the Young’s modulus, and ξ the modal damping ratios. Table 1.3 summarizes the uncertainties in the parameters of reinforced concrete MWFRS with f'_c the concrete compressive strength, f_y the reinforcement strength, and ξ once again the modal damping ratios. All nominal values coincided with those used during the design of the archetype buildings.

Macro parameters

The estimation of Sobol indices is computationally complex and is directly related to the number of random variables in the problem. To avoid defining computationally intractable problems, the concept of macro parameters can be leveraged in which uncertainties are grouped and treated as a single entity in the analysis. The following macro parameters were considered when analyzing the steel archetypes:

Table 1.1: Uncertainties in the gravity and wind loads.

	Mean	COV	Distribution	Reference
D	$1.05D_n^a$	0.1	Normal	[1.10, 1.23]
L_{apt}	$0.24L_n^a$	0.6	Gamma	[1.10, 1.23]
w_1	1.0	b	Normal	[1.18, 1.21]
w_2	1.0	0.05	Normal	[1.3, 1.21]
w_3	1.0	0.05	Normal	[1.3, 1.21]

^a D_n, L_n : Nominal dead load and live load

^b Depends on the record length.

Table 1.2: Description of random variables in steel MWFRS.

	Nominal	$\frac{\text{Mean}}{\text{Nominal}}$	COV	Distribution	Reference
F_y	50 (ksi)	1.1	0.06	Normal	[1.14]
E_s	29000 (ksi)	1	0.04	Lognormal	[1.2, 1.23]
ξ	2%	1	0.3	Lognormal	[1.4]

COV: coefficient of variation

1. Macro parameter 1: Damping: damping ratio ξ ;
2. Macro parameter 2: Material Properties: yield stress, F_y , and Young's modulus, E_s ;
3. Macro parameter 3: Gravity Loads: dead load (including superimposed dead load), D , and arbitrary point in time, L_{apt} ;
4. Macro parameter 4: Record-to-Record Variability: the independent random variables, θ_{ij} , characterizing the stochastic nature of the dynamic wind loads as well as the random variables w_1, w_2 , and w_3 .

When analyzing the reinforced concrete archetypes, the following macro parameters were considered:

1. Macro parameter 1: Damping: damping ratio ξ ;
2. Macro parameter 2: Concrete Material Properties: concrete compressive strength, f'_c (it should be noted that this caused the concrete Young's modulus to become a derived random variable);
3. Macro parameter 3: Reinforcing Steel Material Properties: reinforcement strength, f_y ;
4. Macro parameter 4: Gravity Loads: dead load (including superimposed dead load), D , and arbitrary point in time, L_{apt} ;

Table 1.3: Description of random variables in reinforced concrete MWFRS.

	Nominal	$\frac{\text{Mean}}{\text{Nominal}}$	CoV*	Distribution	Reference
f'_c	10 (ksi)	1.09	0.11	Normal	[1.14]
	12 (ksi)	1.08	0.11	Normal	[1.14]
f_y	60 (ksi)	1.13	0.03	Normal	[1.14]
ξ	2%	1	0.4	Lognormal	[1.12]

COV: coefficient of variation

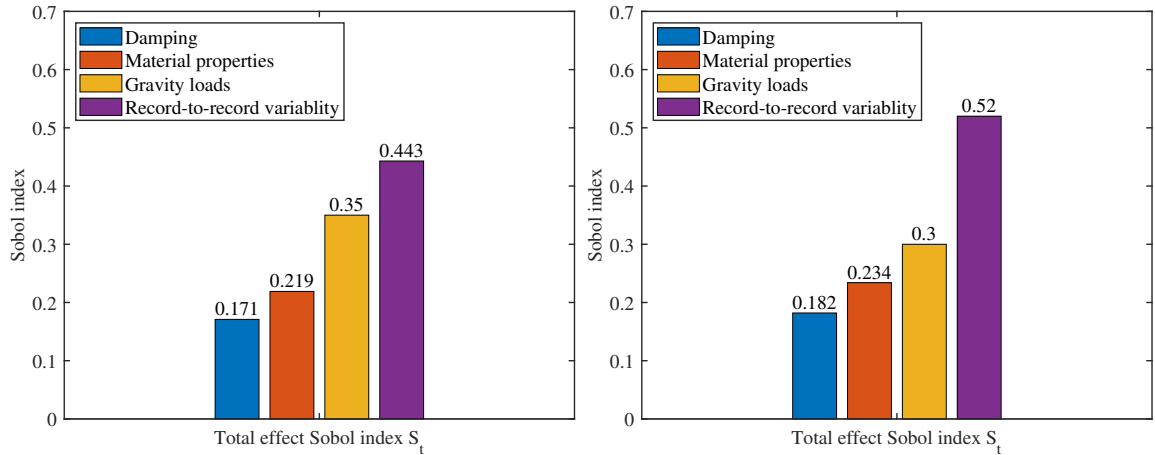
- Macro parameter 5: Record-to-Record Variability: the independent random variables, θ_{ij} , characterizing the stochastic nature of the dynamic wind loads as well as the random variables w_1 , w_2 , and w_3 .

1.3.3 Results

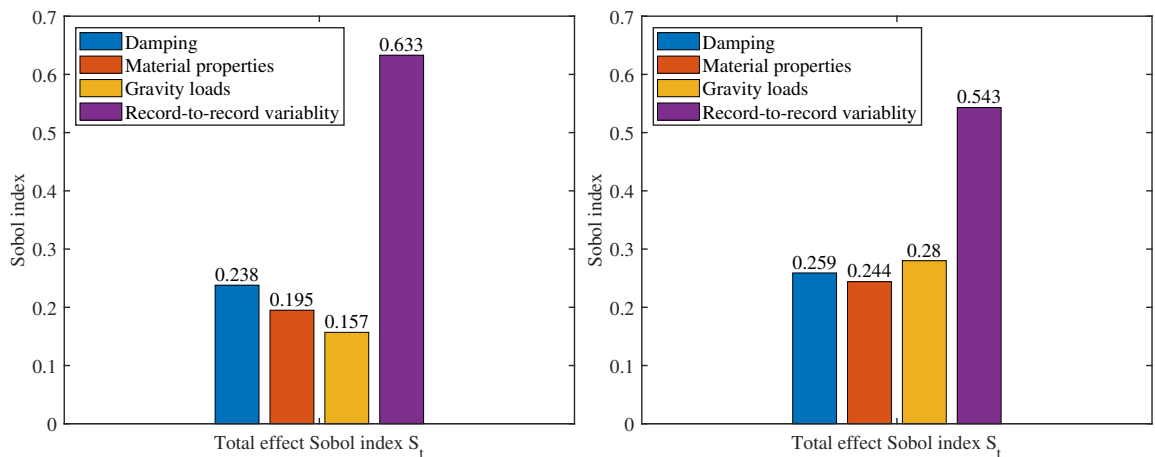
The Sobol indices were estimated for the NY square steel archetype and the NY rectangular concrete core archetype of Sec. 1.1.4. The Miami steel archetype was not considered due to the issues discussed in Sec. 1.1.4. In particular, the interest was on quantifying the importance of record-to-record variability with respect to gravity loads and system parameters as defined by the macro parameters. Therefore, the sensitivity analysis was carried out for a fixed wind direction and wind speed. In particular, the wind speed was fixed as the 700-year design wind speed (multiplied by the directionality factor supplied by CPP). The direction was set to 270° for the NY square steel archetype and the NY rectangular concrete core archetype as this was the critical wind direction as evident from Figs. 1.8 and 1.12.

Figure 1.18 reports the total-effect Sobol index for the maximum DCR and the elastic multiplier (defined as the maximum that the external dynamic wind loads can be amplified before yielding in at least one component occurs) for the NY square steel archetype. As can be seen, for both the maximum DCR and the elastic multiplier, record-to-record variability is responsible for the majority of the observed variability for a given wind speed and direction. Figure 1.19 shows that similar results hold for the maximum (over all floors) interstory drift response in both the alongwind and acrosswind directions. It is interesting to observe that the sensitivity to record-to-record variability would seem to be greater for the interstory drift response than the maximum DCR and the elastic multiplier relative to the material, gravity loads, and damping parameter uncertainties.

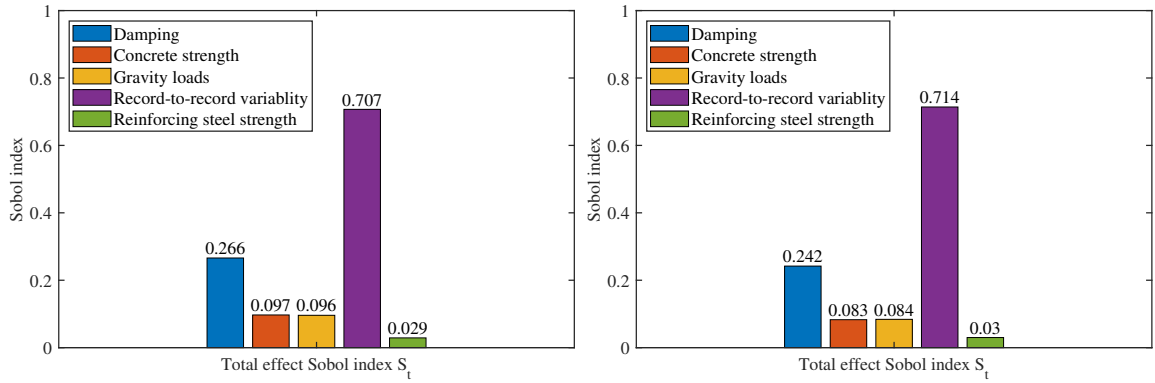
Figures 1.20 and 1.21 reported the analogous results for the NY rectangular concrete core archetype. Similar observations can be made with the caveat that record-to-record variability would seem to play a more important role in creating variability in the maximum DCR and elastic multiplier. However, further analysis would be required to substantiate this finding.



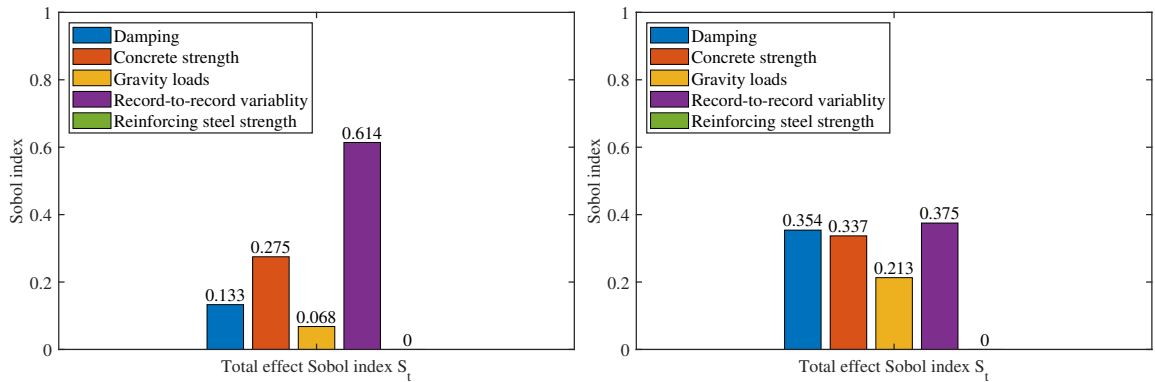
(a) Maximum DCR (b) Elastic multiplier
 Figure 1.18: NY square steel archetype: Total-effect Sobol index for the maximum DCR over and elastic multiplier.



(a) Maximum alongwind drift (b) Maximum crosswind drift
 Figure 1.19: NY square steel archetype: Total-effect Sobol index for the alongwind and crosswind maximum (over the height of the building) interstory drift.



(a) Maximum DCR (b) Elastic multiplier
 Figure 1.20: NY rectangular concrete core archetype: Total-effect Sobol index for the maximum DCR over and elastic multiplier.



(a) Maximum alongwind drift (b) Maximum acrosswind drift
 Figure 1.21: NY rectangular concrete core archetype: Total-effect Sobol index for the alongwind and acrosswind maximum (over the height of the building) interstory drift.

1.4 Concluding Remarks

Record-to-record variability is inherent to any system subject to stochastic excitation. Structural systems subject to dynamic wind loads are not an exception. Traditionally wind engineering has treated the effects of record-to-record variability by considering the expected peak responses, i.e., the average peak response that would be obtained from analyzing the MWFRS under multiple realizations of the dynamic wind loads for each wind speed and direction of interest. This treatment can be traced back to various historical reasons including how for linear elastic systems the expected peaks can be efficiently and elegantly estimated in the frequency domain. Nevertheless, with the interest in wind analysis schemes that use time history analysis, including PBWD, apparent discrepancies can occur. Indeed, current wind time history analysis procedures are generally based (for a multitude of reasons, including reasons related to practical implementation) on the use of a single wind record for each critical wind direction. Unless the record is appropriately scaled, such an approach does not provide a probabilistic treatment of record-to-record variability. This phase of the project demonstrated that record-to-record variability can cause significant variability in the peak responses of the MWFRS. It was seen that the coefficient of variation on the peak responses, specifically demand-to-capacity ratios of the critical components will in general be in the range of 0.1 to 0.3. Through formal sensitivity analysis carried out through the Sobol method, it was shown that record-to-record variability can represent an important system uncertainty. In traditional wind design, this variability is treated by calibrating the ESWLs to expected peaks. Through the analysis of archetype structures, it was shown that this can easily lead to wind records that significantly exceed the wind demand envelopes estimated from ESWLs. If practical, it is recommended that for each wind speed and direction in which time history analysis is to be carried out, a suite of wind records should be considered from which the expected peak responses can be directly estimated as can the variability around the expected value due to record-to-record variability. If running multiple wind records is computationally prohibitive, using a single record that is appropriately scaled to produce the expected peak of a critical response parameter is recommended. Such considerations are important when carrying out nonlinear time history analysis due to its path dependence and therefore sensitivity to individual records.

Bibliography

- [1.1] American Society of Civil Engineers. *Prestandard for Performance-Based Wind Design*. Reston, VA, 2019.
- [1.2] F. M. Bartlett, R. J. Dexter, M. D. Graeser, J. J. Jelinek, B. J. Schmidt, and T. V. Galambos. Updating standard shape material properties database for design and reliability. *Engineering Journal*, 40:2–14, 2003.
- [1.3] R. Bashor, T. Kijewski-Correa, and A. Kareem. On the wind-induced response of tall buildings: the effect of uncertainties in dynamic properties and human comfort thresholds. In *10th Americas Conference on Wind Engineering*, 2005. CD-ROM.
- [1.4] E. Bernardini, S. M. J. Spence, D.-K. Kwon, and A. Kareem. Performance-based design of high-rise buildings for occupant comfort. *Journal of Structural Engineering*, 141(10):04014244, 2015.
- [1.5] X. Chen and A. Kareem. Proper orthogonal decomposition-based modeling, analysis, and simulation of dynamic wind load effects on structures. *Journal of Engineering Mechanics*, 131(4):325–339, 2005.
- [1.6] W. C. Chuang and S. M. J. Spence. A framework for the efficient reliability assessment of inelastic wind excited structures at dynamic shakedown. *Journal of Wind Engineering and Industrial Aerodynamics*, page 104834, 2022.
- [1.7] A. G. Davenport. Note on the distribution of the largest value of a random function with application to gust loading. *Proceedings, Institution of Civil Engineering*, 28:187–196, 1964.
- [1.8] G. Deodatis. Simulation of ergodic multivariate stochastic processes. *Journal of Engineering Mechanics*, 122(8):778–787, 1996.
- [1.9] T. G. A. Duarte, A. Arunachalam, A. Subgranon, and S. M. J. Spence. Uncertainty quantification and simulation of wind-tunnel-informed stochastic wind loads. *Wind*, 3(3):375–393, 2023.

-
- [1.10] B. R. Ellingwood, J. G. MacGregor, T. V. Galambos, and C. A. Cornell. Probability based load criteria: Load factors and load combinations. *Journal of the Structural Division*, 108:978–997, 1982.
- [1.11] M. Giofrè, V. Gusella, and M. Grigoriu. Non-gaussian wind pressure on prismatic buildings. I: Stochastic field. *Journal of Structural Engineering*, 127(9):981–989, 2001.
- [1.12] J. Healey, S. Wu, and M. Murga. *Structural building response review. NUREG/CR1423, vol. I*. US Nuclear Regulatory Commission, Washington, DC, 1980.
- [1.13] M. Liu, X. Chen, and Y. Yang. Estimation of peak factor of non-gaussian wind pressures by improved moment-based hermite model. *Journal of Engineering Mechanics*, 143(7), 2017.
- [1.14] A. S. Nowak and K. R. Collins. *Reliability of Structures*. CRC Press, 2013.
- [1.15] Z. Ouyang and S. M. J. Spence. A performance-based damage estimation framework for the building envelope of wind-excited engineered structures. *Journal of Wind Engineering and Industrial Aerodynamics*, 186:139–154, 2019.
- [1.16] Z. Ouyang and S. M. J. Spence. A performance-based wind engineering framework for engineered building systems subject to hurricanes. *Frontiers in Built Environment*, page 133, 2021.
- [1.17] L. Peng, G. Huang, X. Chen, and A. Kareem. Simulation of multivariate non-stationary random processes: Hybrid stochastic wave and proper orthogonal decomposition approach. *Journal of Engineering Mechanics*, 143(9), 2017.
- [1.18] F. Sadek, S. Diniz, M. Kasperski, M. Giofrè, and E. Simiu. Sampling errors in the estimation of peak wind-induced internal forces in low-rise structures. *Journal of Engineering Mechanics*, 130(2):235–239, 2004.
- [1.19] I. M. Sobol. Global sensitivity indices for nonlinear mathematical models and their monte carlo estimates. *Mathematics and Computers in Simulation*, 55(1-3):271–280, 2001.
- [1.20] S. M. J. Spence and A. Kareem. Data-enabled design and optimization (DEDOpt): tall steel building frameworks. *Computers & Structures*, 129:134–147, 2013.
- [1.21] S. M. J. Spence and A. Kareem. Performance-based design and optimization of uncertain wind-excited dynamic building systems. *Engineering Structures*, 78:133–144, 2014.
-

-
- [1.22] A. Suksuwan and S. M. J. Spence. Performance-based design optimization of uncertain wind excited systems under system-level loss constraints. *Structural Safety*, 80:13–31, 2019.
- [1.23] H. Zhang, B. R. Ellingwood, and K. J. R. Rasmussen. System reliabilities in steel structural frame design by inelastic analysis. *Engineering Structures*, 81:341–348, 2014.
- [1.24] H. Zhao, M. Grigoriu, and K. R. Gurley. Translation processes for wind pressures on low-rise buildings. *Journal of Wind Engineering and Industrial Aerodynamics*, 184:405–416, 2019.
-

Chapter 2

Phase 2: Uncovering the reasons behind the apparent discrepancy between target and achieved reliability

Initial reliability studies have suggested that there is a discrepancy between the reliabilities obtained from systems designed to comply with current LRFD procedures for steel and reinforced concrete MWFRS and the target reliabilities indicated in Table 1.3-1 of ASCE 7-22. This discrepancy has been observed as a general trend to miss target reliabilities in deficit as compared to the values indicated in Table 1.3-1. Phase 2 of this project focused on identifying the underlying reasons for this apparent discrepancy. This was achieved by first explicitly estimating the reliability of the MWFRS of archetype buildings of phase 1 of this project using the WiRA modeling environment outlined in [2.10] which is consistent with many current PBWD approaches [2.24]. In particular, only the NY square steel archetype and the NY rectangular concrete core archetype were considered as these were the only buildings that passed the QA/QC of Phase 1. Deterministic sensitivity analysis was then conducted to identify the sensitivity of the reliability estimated to the choices defining the wind climates and building aerodynamics. Subsequently, the historical developments underpinning Table 1.3-1 were critically reviewed and compared to those underpinning explicit reliability modeling therefore identifying the underlying reasons for the apparent discrepancy in achieved and target reliability for MWFRS designed with building-specific climatological and aerodynamic studies.

2.1 Explicit reliability estimation by WiRA

2.1.1 The reliability problem

Problem definition

In general, the probability of failure of a system concerning a limit state of interest can be written in the following form [2.2]:

$$P_f = P(g(\mathbf{Y}) \leq 0) = \int \cdots \int_{g(\mathbf{Y}) \leq 0} f_{\mathbf{Y}}(\mathbf{y}) d\mathbf{y} \quad (2.1)$$

where \mathbf{Y} is a vector collecting the basic random variables associated with both model and load uncertainties (in the following, uppercase notation will be used to indicate the random variable while lowercase notation will be used to indicate a realization); $f_{\mathbf{Y}}$ is the joint probability density function of \mathbf{Y} ; while g is a general limit state function that assumes negative values upon the exceedance of a limit state of interest, e.g. failure to reach the state of dynamic shakedown [2.26, 2.7]. From a classic first order reliability method (FORM) assumption (i.e., linear limit state function in the independent standard normal space), P_f can be transformed into a direct estimate of the reliability of the system with respect to g through:

$$\beta = \Phi^{-1}(1 - P_f) \quad (2.2)$$

where β is the classic reliability index [2.22]. The evaluation of Eq. (2.1), and subsequently the reliability index of Eq. (2.2), within the context of this work requires the identification of: 1) an appropriate set of limit states to consider together with the system-level limit state of dynamic shakedown; 2) an appropriate set of model and load uncertainties for defining \mathbf{Y} , discussed in Sec. 2.1.2; and 3) an appropriate solution strategy for solving Eq. (2.1) that can handle the inevitably high-dimensions of \mathbf{Y} , as well as the small probabilities generally associated limit states such as dynamic shakedown, discussed in Sec. 2.1.3.

The limit states

For characterizing the reliability of the system within the context outlined above, the following limit states will be considered:

1. LS1: component-level first yield limit states (i.e. traditional limit states used in current design);
2. LS2: system-level first yield limit state;
3. LS3: system-level dynamic shakedown limit state;

Failure associated with LS1 can be defined for the j th component of the discretization through the limit state function:

$$g_j^{(LS1)}(\mathbf{y}) = \max_{1 \leq i \leq N_{I_j}} \left\{ \mathbf{R}_j(x_i; \mathbf{y}) - \max_{0 \leq t \leq \bar{T}} [\mathbf{N}_{ji}^T(\mathbf{y}) \mathbf{D}_{s_j}(x_i; t, \mathbf{y})] \right\} \quad (2.3)$$

where $\mathbf{D}_{s_j}(x_i; t, \mathbf{y})$, for $i = 1, \dots, N_{I_j}$, is the vector of time varying stress-resultants at each integration point along the element that must take into account any stress redistribution caused by yielding elsewhere in the structure.

For LS2 and LS3, failure can be directly identified in terms of the elastic dynamic shakedown multipliers, s_e and s_p respectively, through the limit state functions: $g^{(LS2)}(\mathbf{y}) = s_e(\mathbf{y}) - 1$ and $g^{(LS3)}(\mathbf{y}) = s_p(\mathbf{y}) - 1$. Indeed, $s_e \leq 1$ indicates how in at least one integration point of the discretization yielding will occur for the unamplified loads while $s_p \leq 1$ implies that under the unamplified loads the structure will not reach a state of dynamic shakedown.

2.1.2 Model and load uncertainties

Model uncertainties

Among the model uncertainties of primary importance are those associated with the mechanical properties of the members. For the stress-resultant model of this work, these include the yield strength, F_{y_j} , of the steel members, as well as the concrete compressive strength, f'_{c_j} , and reinforcing steel yield strength, f_{y_j} , of the reinforced concrete members. In addition, uncertainty in the stiffness of the system is modeled by treating the young's modulus of each member as random. In particular, for steel members, the young's modulus can be taken as a basic random variable, E_{s_j} , while for concrete members, it can be treated as derived from the randomness in f'_{c_j} . These basic random variables create uncertainty in not only the structural stiffness \mathbf{K} , and consequently the natural frequencies of the system, but also the yield domains associated with each integration point of each member through randomizing the plastic resistance vector, $\mathbf{R}_j(x_i)$, as well as the external unit normals, collected in the matrix \mathbf{N}_{ji} , of each yield surface. For dynamic systems, such as those of interest to this work, the uncertainty in inherent damping must also be modeled. A straightforward approach, and that will be followed in this work, is to take the model damping ratios, ξ_k , of Eq. (1.8) as basic random variables.

Climate model uncertainties

To capture wind directionality effects, a sector-by-sector approach [2.14, 2.15] is adopted. The site-specific wind climate is therefore characterized by dividing it into a number of wind direction sectors, typically 8 to 16 [2.14, 2.15]. For each sector, the intensity of the wind hazard is measured in terms of the largest time-averaged (over the storm duration T) wind speed, v_H , to occur at a height of interest H (e.g.

building height) over the lifespan of the structure (e.g. 50 years). Uncertainty in v_H is captured through the following lifespan complementary cumulative distribution function (CCDF):

$$G_n(v_H) = 1 - [F_{V_H}(v_H|n)]^y \quad \text{for } n = 1, \dots, N_{\text{sec}} \quad (2.4)$$

where $F_{V_H}(v_H|n)$ is the annual probability distribution function associated with the largest mean annual wind speeds to occur in sector n , y is the number of years defining the lifespan of the structure, while N_{sec} is the total number of sectors. To model the variation of wind direction within a given sector, the knowledge of the sectorial conditional CCDF of wind direction, α , given v_H , $G_n(\alpha|v_H)$, would be needed. The determination of $G_n(\alpha|v_H)$ requires the knowledge of the joint probability of wind direction and speed in sector n , a term for which there is seldom enough information available for estimation. As a consequence, the variation of wind direction in a given sector will be taken as independent of sectorial wind speed and governed by a uniform probability distribution.

It should be observed that, inherent to $F_{V_H}(v_H|n)$, are uncertainties associated with both observational and sampling errors as well as aspects such as differences in roughness between the meteorological stations and the site of interest. As a consequence, the estimation of $F_{V_H}(v_H|n)$ generally requires a certain amount of engineering judgment, especially if the partial correlation between the sectorial wind speeds is to be accounted for during the estimation of the reliability of the system.

Aerodynamic model uncertainties

Given a wind speed v_H and direction α for which the evaluation of the limit states of Sec. 2.1.1 is desired, an appropriate aerodynamic model is required for estimating the dynamic loads, $\mathbf{F}(t; v_H, \alpha)$, acting on the system during the storm of duration T . The path-dependent nature of inelastic analysis requires that $\mathbf{F}(t; v_H, \alpha)$ includes an appropriate ramp up and ramp down at the beginning and end of the wind event. As suggested in [2.9], this can be achieved through an appropriate envelope function, $e(t)$, such that:

$$\mathbf{F}(t; v_H, \alpha) = e(t)\mathbf{f}(t; v_H, \alpha) \quad (2.5)$$

where $\mathbf{f}(t; v_H, \alpha)$ is a stationary representation of $\mathbf{F}(t; v_H, \alpha)$. A simple choice for $e(t)$, and that is suggested in [2.16, 2.17, 2.19, 2.9], is the following linear ramp:

$$e(t) = \begin{cases} t/T_1, & t \in [0, T_a] \\ 1, & t \in [T_a, T_b] \\ 1 - (t - T_b)/T, & t \in [T_b, T] \end{cases} \quad (2.6)$$

where T_a and T_b define the length of the ramp (e.g. 2 minutes).

The generality of the model of Eq. (2.5) depends on $\mathbf{f}(t; v_H, \alpha)$ that must be able to: 1) capture the generally complex and building specific aerodynamics, e.g.

vortex shedding and detached flow, associated with high-rise buildings; and 2) the record-to-record variability, i.e. stochasticity, of the dynamic winds loads. To this end, in this work, the modeling of $\mathbf{f}(t; v_H, \alpha)$ is based on the wind tunnel informed spectral proper orthogonal decomposition (POD) model outlined in [2.25, 2.8] and described in Chapter 1 of this report.

Gravity load uncertainties

Together with the wind loads, appropriate probabilistic models for treating the uncertainty in the dead and superimposed dead loads, generally combined into a single dead load D , as well as live load, are required. Consistently with how reliability is estimated for systems subject to extreme wind events [2.12, 2.27], the “arbitrary point-in-time” live load, L_{apt} , should be considered for combination with the stochastic winds loads of Section 1.1.3. In general, the probabilistic modeling of these gravity loads can be directly related to their nominal values [2.12, 2.27]. For example, in this work, the probabilistic dead and live loads are related to the nominal values suggested in [2.1] through the distributions outlined in Table 2.1.

Table 2.1: Distribution parameters used for modeling the uncertainty in the gravity loads.

	Mean	COV	Distribution	Reference
D	$1.05D_n^a$	0.1	Normal	[2.12, 2.27]
L_{apt}	$0.24L_n^b$	0.6	Gamma	[2.12, 2.27]

^a D_n : Nominal combined dead and superimposed dead load [2.1]
^b L_n : Nominal live load [2.1]

2.1.3 Stochastic simulation scheme

To solve for the failure probability associated with each limit state through the integral of Eq. (2.1), direct Monte Carlo (MC) simulation would fast become computationally infeasible due to: 1) the computationally intensive nature of inelastic analysis of large scale systems; and 2) the need to simulate rare events for which MC methods are known to be inefficient. To overcome the aforementioned difficulties, a stratified sampling scheme, based on that recently proposed in [2.20, 2.21, 2.3, 2.4], is adopted in this work. In particular, the scheme is embedded with a sector-by-sector approach for modeling the effects of wind directionality. The failure probability of the system with respect to any one of the limit states of Sec. 2.1.1 is therefore given by:

$$P_f = \max_{1 \leq n \leq N_{\text{sec}}} [P_{f_n}] \quad (2.7)$$

where P_{f_n} is the failure probability of the system for wind events occurring in sector n . To evaluate P_{f_n} , and subsequently P_f through Eq. (2.7), the basic idea is to use

the sectorial wind speeds, $v_H|n$, as the stratification variable. The sectorial failure probabilities can then be directly estimated using the stratified sampling schemes detailed in [2.3].

2.2 Explicit reliability results

2.2.1 Problem setup

As mentioned in the introduction to this Chapter, only the NY square steel archetype and the NY rectangular concrete core archetype were considered in the reliability study of this project as these were the only buildings that passed the QA/QC of Phase 1. To define the site-specific wind hazard curve for NY, the annual 3 s gust wind speeds, v_3 , corresponding to mean recurrence intervals (MRIs) of 300, 700, 1700, 3000, 10,000, 100,000, and 1,000,000 years for New York City, obtained from the wind hazard maps under development for ASCE 7-22, were first transformed to the site-specific annual mean hourly wind speeds at the reference height ($H=182.88$ m) based on the ESDU methodology as provided by CPP. These wind speeds were then fitted to a Type I distribution (consistently with the ASCE 7-22 wind maps) for modeling the non-directional annual wind speed distribution, $F_{V_H}^{(nd)}$, from which the non-directional annual wind hazard was obtained and subsequently the corresponding non-directional hazard curve for a lifespan of $y = 50$ years.

For implementing the sector-by-sector approach, eight sectors, specifically N, NE, E, SE, S, SW, W, and NW were considered. The sectorial probability distributions of largest mean annual wind speeds, $F_{V_H}(v_H|n)$, where defined through directional factors, κ , such that: $F_{V_H}(v_H|n) = F_{V_H}^{(nd)}(v_H/\kappa_n)$, i.e. the sectorial wind speeds were linearly related to the non-directional wind speeds. Appropriate directional factors for New York and ASCE 7-22 Risk Category II designs (target Risk Category used for the design of the archetypes) were provided by the project partner Cermak Peterka Petersen (CPP) for each sector, and are summarized in Table 2.2. Consistently with the scaled sector approach, to account for the partial correlation of the wind speeds occurring in different sectors, the raw directional factors were increased by CPP in order to have at least one sector that has a directional factor of unity.

Wind tunnel data for calibration of the stochastic wind load model of Chapter 1, was also provided by CPP. During the wind tunnel tests, data was collected for a sampling frequency of 250 Hz and a total recorded duration of 81.92 s. Datasets associated with 36 wind directions ($\alpha = \{0^\circ, 10^\circ, \dots, 340^\circ, 350^\circ\}$) were measured and scaled therefore defining a wind tunnel realization of $\mathbf{F}(t)$. To calibrate the stochastic model of Section 1.1.3, the first 25 spectral eigenvalues and modes were extracted from the wind tunnel realization of $\mathbf{F}(t)$ (25 spectral modes have been seen to be adequate for representing the energy of dynamic wind forces acting on high-rise buildings [2.11]). The total duration of the stationary segment of the wind

Table 2.2: Values of κ for different wind direction sectors.

Sector	N	NE	E	SE	S	SW	W	NW
κ	0.88	0.88	0.84	0.84	0.84	0.88	1.00	0.92

events was taken as 1 hour, i.e. $T_b - T_a = 3600$ s, to which a 2-minute ramp up and ramp down was added through the envelope function of Eq. (2.6). The total duration of the simulated realization of $\mathbf{F}(t)$ was therefore 3840 s. A constant sampling frequency of 2 Hz was considered for all realizations of the stochastic wind model. Because the duration of the simulated wind loads was greater than 1 hour at full scale, w_1 was taken to have a coefficient of variation (COV) of 0.075 [2.23, 2.5].

The reliability assessment was carried out considering a lifespan of 50 years, i.e. $y = 50$ in Eq. (2.4). To calibrate the framework eight strata were considered for each wind sector. Because the sectorial wind speeds are linearly related to the non-directional wind speeds through the factors of Table 2.2, stratification was carried directly in terms of the non-directional 50-year hazard curve. The lower bound wind speed of the eighth strata was fixed by calibrating it to the wind speed associated with the target probability of failure for a Risk Category II building (i.e., the mean hourly wind speed associated with an annual probability of failure of 3.0×10^{-5}). The bounds of the intermediate strata were identified through the procedures outlined in [2.3]. The distributions used for the uncertain parameters follow those outlined in Chapter 1 Section 1.3.2.

2.2.2 Results

Tables 2.3 and 2.4 report the sector reliabilities for component first yield (LS1) for the critical component (i.e., the component with smallest reliability) of the NY square steel archetype and the NY rectangular concrete core archetype. As can be seen, both archetypes are most sensitive to winds from the west (sector W) where the minimum component reliability for the steel archetype is 2.30 while the minimum reliability for the concrete core archetype is 2.61. The difference in the critical component reliability between the two archetype can be traced back to how the NY steel archetype design was closer to the LFRD limit states than the NY rectangular concrete core archetype (See results of Chapter 1, Sec. 1.2.2). When interpreting these results it is important to recall how the sector failure probabilities of Eq. (2.7) are statistical estimates over sample sets generated in accordance with random sampling theory, i.e., samples are independent and identically distributed for each sector, as illustrated in Fig. 2.1 for the damping ratios, ξ , where no bias in samples are seen for any particular sector. Figures 2.2 and 2.3 report the component first yield reliability (LS1) for all components for winds blowing down the critical sector, W, for the NY square steel archetype and the NY rectangular concrete core archetype. By recalling how both archetypes were designed to satisfy LFRD

requirements for a Risk Category II building, the target reliability according to Table 1.3-1 of ASCE 7-22 is 3.0. There is, therefore, a significant apparent deficit in reliability. When considering these results, it is important to observe the following:

1. The wind hazard curve was explicitly calibrated to the point value wind speeds suggested in ASCE 7-22;
2. The wind hazard curve was assumed to follow a Type I distribution which is consistent with the construction of the ASCE wind hazard maps;
3. The directionality factors used in the scaled sector approach were estimated by CPP using best practices for this type of approach;
4. The LRFD designs used wind tunnel estimated ESWLs that were based on post-processing of the same raw wind tunnel data used to calibrate the stochastic wind load model used to represent the record-to-record variability in the dynamic wind loads;
5. All distributions used to characterize the uncertainty in the model parameters and gravity loads were carefully chosen to comply with those used in developing the target reliabilities of the ASCE 7-22.

In addition, by observing the two archetypes were carefully designed to meet the LRFD requirements using the relevant ASCE 7-22 load combinations and were thoroughly checked through the QA/QC process discussed in Chapter 1 Section 1.1.4, the likelihood the observed discrepancies can be attributed to modeling errors or treatment of uncertainty that is inconsistent with that underpinning ASCE 7-22 would seem negligible. The following sections of this Chapter will explore possible reasons for the discrepancies observed in this section.

Before closing this section, it is interesting to observe that the system level first yield reliability (LS2) for the critical sector, W, was 2.30 and 2.57 for the steel and reinforced concrete archetypes which highlight how often the same component will yield first. In addition, for the critical sector (W), the shakedown reliability of the two archetypes is 3.11 (steel) and 3.19 (reinforced concrete) illustrating how both MWFRS have significant inelastic reserves before shakedown will no longer be achieved. It is also interesting to observe that the system-level yielding expected at shakedown is similar to that required in the system in order to roughly meet the target reliabilities of Table 1.3-1 for a Risk Category II building.

At this point, it is warranted to discuss the role of damping. In particular, it is of interest whether the reliability indexes of 2.30 and 2.61 could be attributed to a combination of very low damping and an across-wind type response, given that the critical sector for both archetypes is parallel to one of the building faces. To investigate this, the reliability analyses were rerun while fixing the damping ratio at 2%, i.e., the damping ratio used in developing the ESWLs. This resulted in only a small change in the component reliability (LS1) within the critical sector, increasing

Table 2.3: NY square steel archetype: LS1 reliability index of the critical component for each wind sector.

Sector	N	NE	E	SE	S	SW	W	NW
β	2.63	3.43	2.98	3.51	3.14	3.56	2.30	2.98

Table 2.4: NY rectangular concrete core archetype: LS1 reliability index of the critical component for each wind sector.

Sector	N	NE	E	SE	S	SW	W	NW
β	3.04	3.37	3.34	3.51	3.23	3.28	2.61	3.30

from 2.30 to 2.31 for the steel archetype and from 2.61 to 2.75 for the reinforced concrete archetype. The relatively larger increase in reliability observed for the reinforced concrete archetype can be attributed to the fact that the coefficient of variation (COV) for the damping ratio of the reinforced concrete archetype was set at 0.4, as suggested in [2.13], as opposed to 0.3 for the steel structure, as suggested in [2.6]. The effect of this can be graphically visualized by comparing Fig. 2.4 with Fig. 2.5, which present a comparison of the elastic multiplier, S_e , in scenarios of random versus fixed damping for the two archetype structures. Note that the elastic multiplier represents the factor by which the external loads must be multiplied for LS1 to be exceeded in at least one element. The critical value of S_e is 1, indicating the transition between an elastic system ($S_e > 1$) and a system in which one or more elements exceed LS1 ($S_e < 1$). From Fig. 2.4, there is only a slight tendency for the S_e values to be smaller in the case of random damping for the steel archetype; that is, the data points tend to fall below the 1-1 line. This tendency is more pronounced for the reinforced concrete archetype, as shown in Fig. 2.5, leading to a more evident increase in reliability.

The component reliability's relative insensitivity to damping can be understood by acknowledging that wind speed is the dominant random variable. Consequently, the most likely failure samples will occur at high wind speeds, regardless of the values assumed by the other random variables. In other words, while a relatively low wind speed coupled with a very small damping value could potentially create large responses, this scenario is much less likely than encountering large responses at a relatively high wind speed paired with an arbitrary damping value. This is highlighted in Fig. 2.6, which shows the sample values of S_e for cases where $S_e < 1$, plotted against the associated damping values for the steel archetype. No evident relationship is observed between low damping values and small S_e values. Similarly, Fig. 2.7 illustrates a comparable situation for the reinforced concrete archetype.

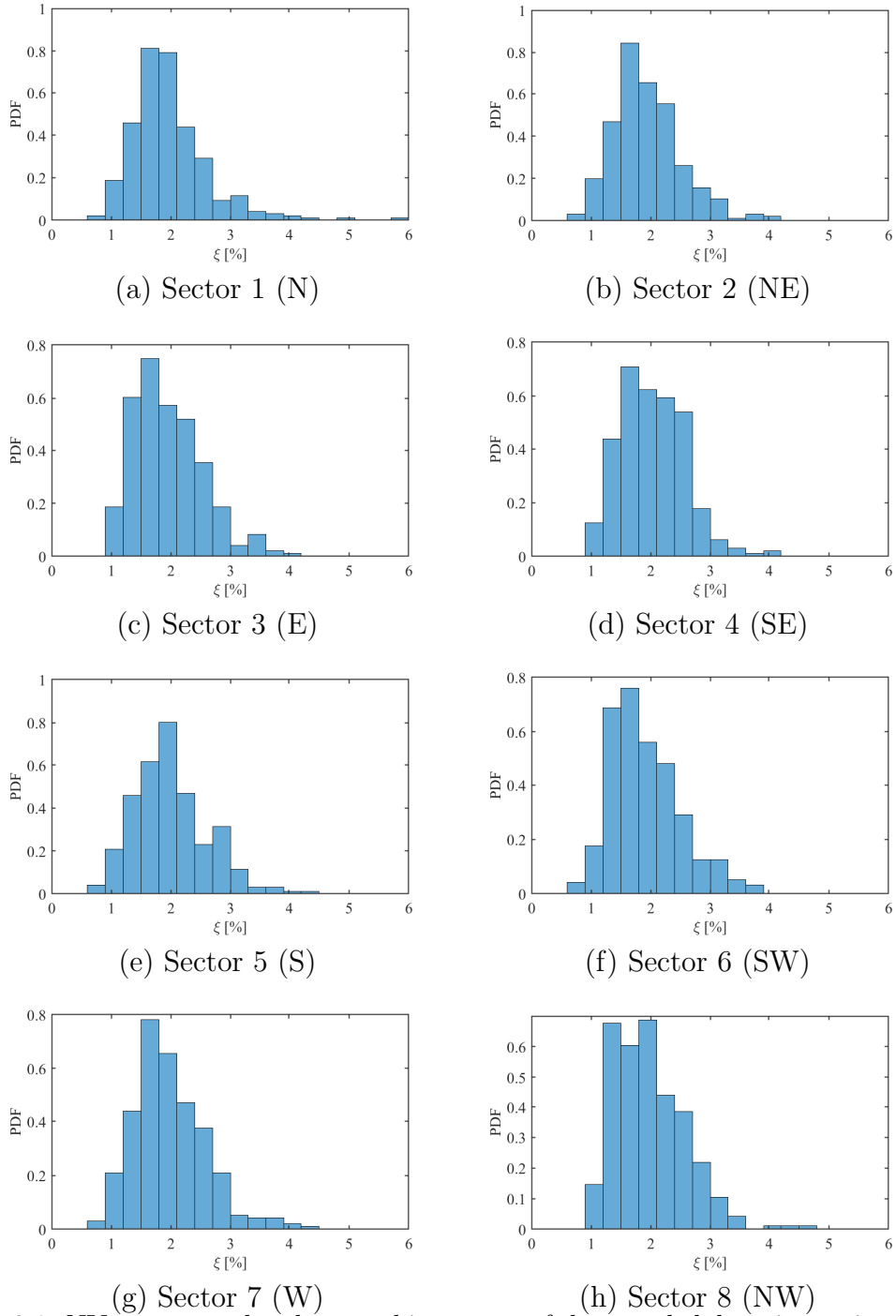


Figure 2.1: NY square steel archetype: histograms of the sampled damping ratios for each sector.

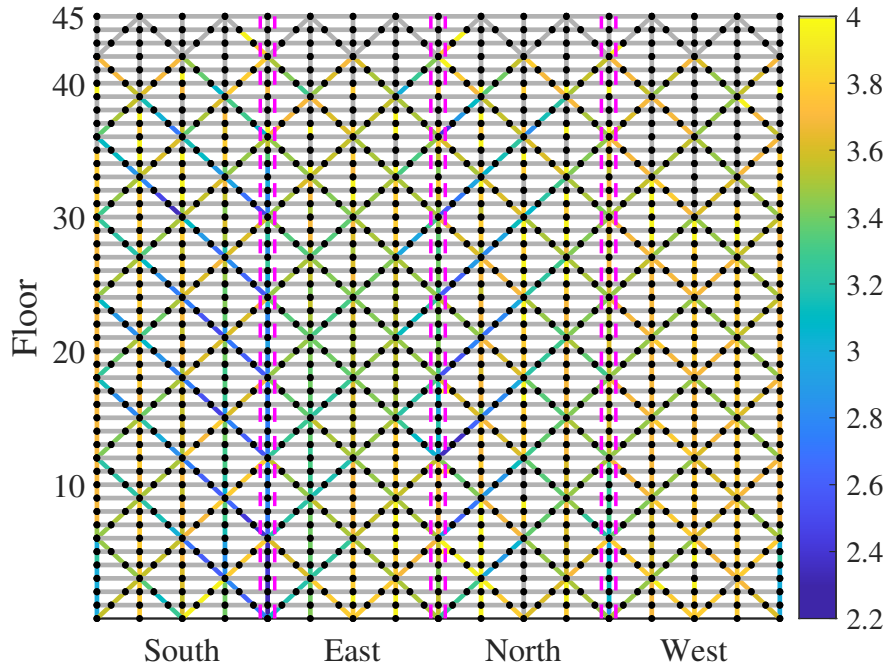


Figure 2.2: NY square steel archetype: Component reliability (LS1).

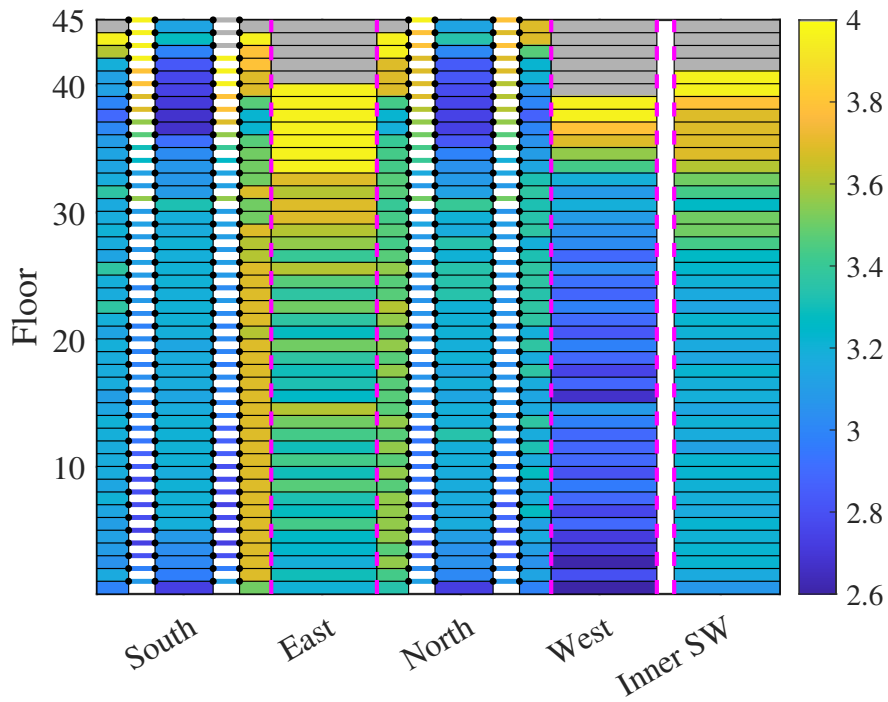


Figure 2.3: NY rectangular concrete core archetype: Component reliability (LS1).

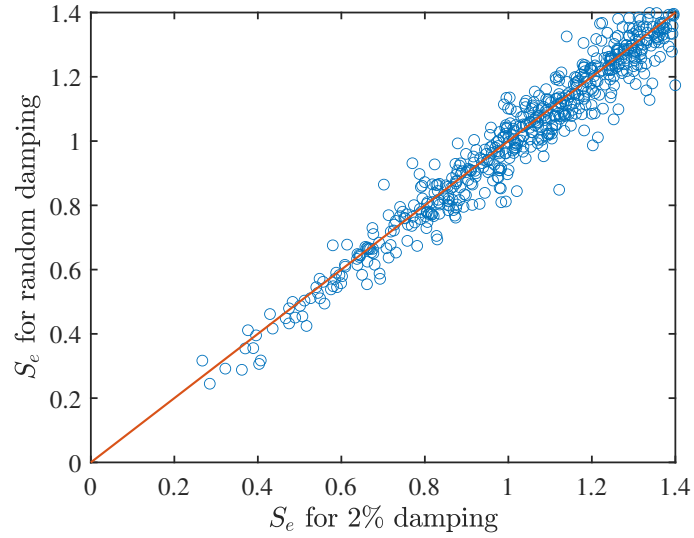


Figure 2.4: NY square steel archetype: elastic multiplier, S_e , estimated for random damping and a fixed damping of 2% ($S_e < 1.4$ shown).

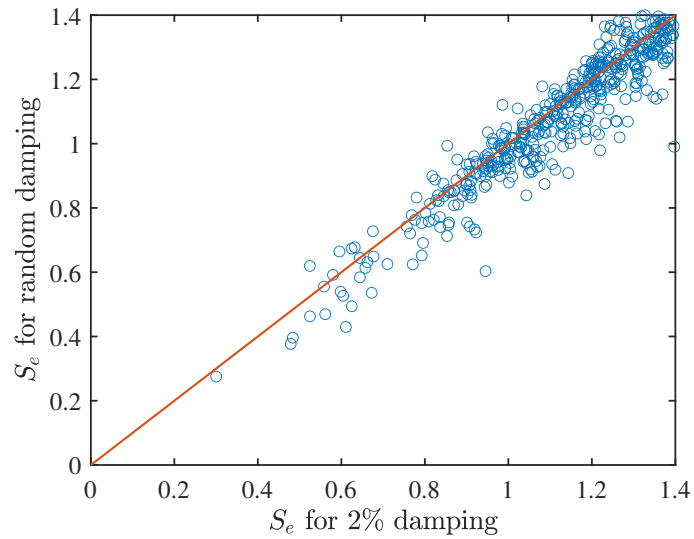


Figure 2.5: NY rectangular concrete core archetype: elastic multiplier, S_e , estimated for random damping and a fixed damping of 2% ($S_e < 1.4$ shown).

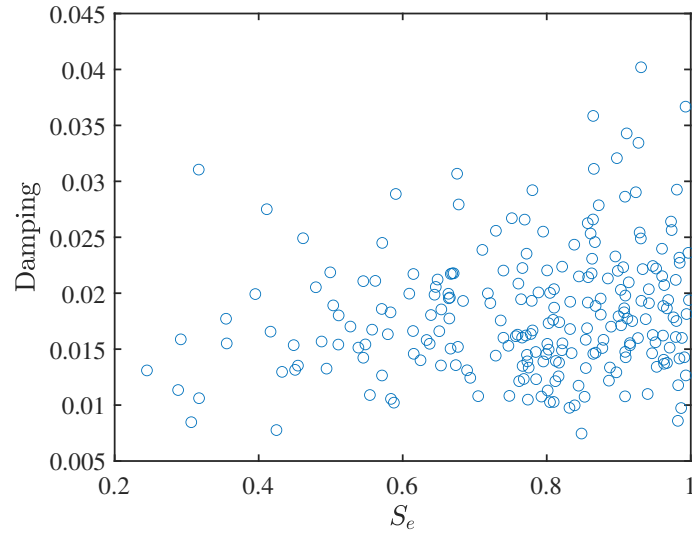


Figure 2.6: NY square steel archetype: $S_e < 1$ values vs random damping.

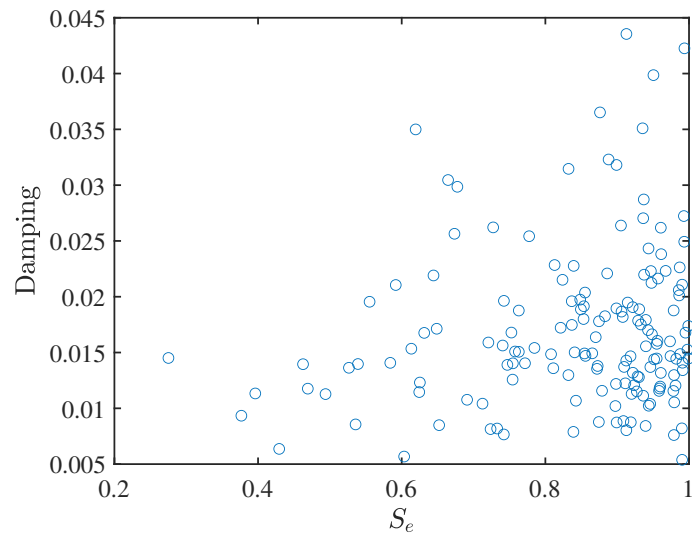


Figure 2.7: NY rectangular concrete core archetype: $S_e < 1$ values vs random damping.

2.3 Sensitivity to climatological and aerodynamic modeling choices

The reliability results of the previous section depend, among other things, on the assumption that the largest wind speeds to occur in the service life of the MWFRS (50 years) follow a Type I distribution (consistently with the ASCE 7-22). In addition, as was noted in the Chapter 1, the stochastic wind load model used in this project captures the non-Gaussian features in the external dynamic wind loads. However, there is little information on whether this makes an appreciable difference to the reliability of the MWFRS. To investigate this as well as the influence of choosing a Type I distribution for modeling the non-directional largest wind speeds to occur in the service life of the MWFRS, a deterministic sensitivity analysis was carried out that centered on the differences observed in the reliability for the following analysis cases:

1. AC1: Type I distribution for the non-directional largest wind speeds and Gaussian loads;
2. AC2: Weibull distribution for the non-directional largest wind speeds and non-Gaussian loads;

These cases were compared to the baseline case corresponding to prevailing practice used in Sec. 2.2.2 and defined using a Type I distribution for the non-directional largest wind speeds and non-Gaussian loads.

Figures 2.8 and 2.9 illustrate the difference in reliability for LS1 (component yield) for AC1 and AC2. As can be seen from Fig. 2.8, while the neglect of non-Gaussian features in the external dynamic wind loads can lead to differences in component reliability as high as 0.25, the reliability of the critical component (component with lowest reliability index) does not show appreciable change (2.31 vs 2.30). It should be observed that as the reliability index increases, greater sample variability in the estimated value of the index will inevitably occur. This should be kept in mind when discussing the variability observed in this section. The difference between a Weibull and Type I distribution of the non-directional largest wind speeds fitted to the point data of the ASCE 7-22 wind hazard maps is illustrated in Fig. 2.10 for the building reference height and exposure. As can be seen, for wind speeds with 50-year probabilities up to 10^{-3} little difference is seen after which the Weibull distribution will give noticeably smaller estimates of the wind speeds. These differences in the wind speed distribution can cause differences in the reliability as high as 0.4, as reported in Fig. 2.9. However, little difference is seen in the reliability of the critical component (2.35 vs 2.30) or the reliability against shakedown (3.27 vs 3.11) as the wind speeds causing the exceedance of these limit states tend to be centered around the wind speeds where the distributions are similar.

Overall, the deterministic sensitivity analysis of this section illustrated how the choice of extreme distribution of the wind speeds did not noticeably affect the rela-

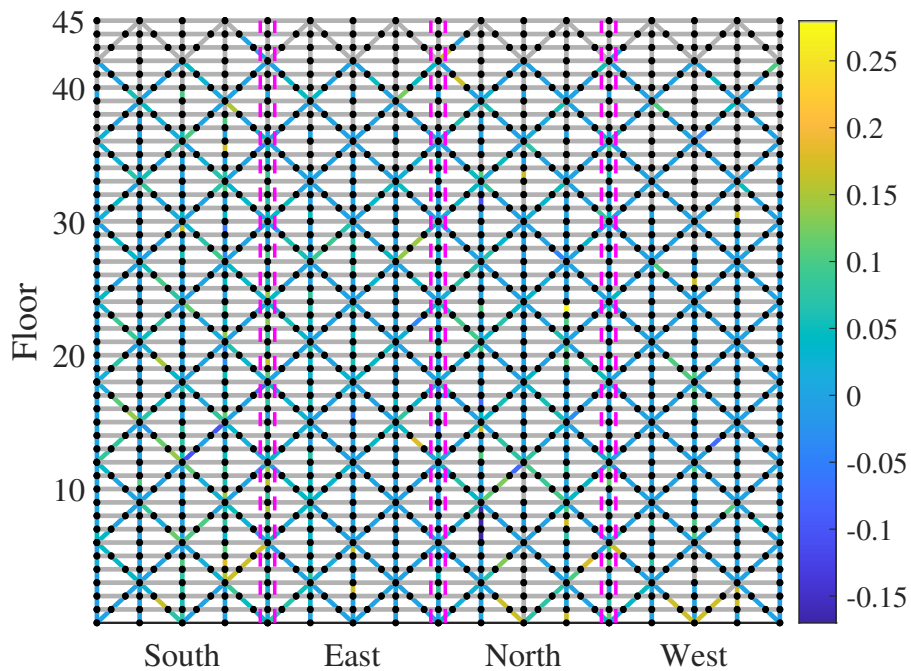


Figure 2.8: NY square steel archetype: LS1 reliability difference between AC1 and the baseline case.

bility of the critical component or the reliability of the MWFRS against shakedown nor did the inclusion/exclusion of non-Gaussian effects. The sensitivity analysis of this section was carried out only for the NY square steel archetype as there is no theoretical reason to expect different results for the NY rectangular concrete core archetype.

2.4 Classic reliability estimates and comparison to explicit reliability modeling

2.4.1 Reliability calculations underpinning LRFD

Preamble

The target reliability for each Risk Category of the ASCE 7-22 is reported in Table 1.3-1 of the standard. In particular, for a Risk Category II building and limit states that “Failure that is not sudden or does not lead to widespread progression of damage”, i.e. LS1 of the two archetypes of this Chapter, a reliability of 3.0 should be achieved if the designs meet all the LRFD design requirements of the governing material code, as do the two archetypes of this Chapter. However, as discussed in Section 2.2.2, the reliability estimated for the two archetypes and LS1 did not meet

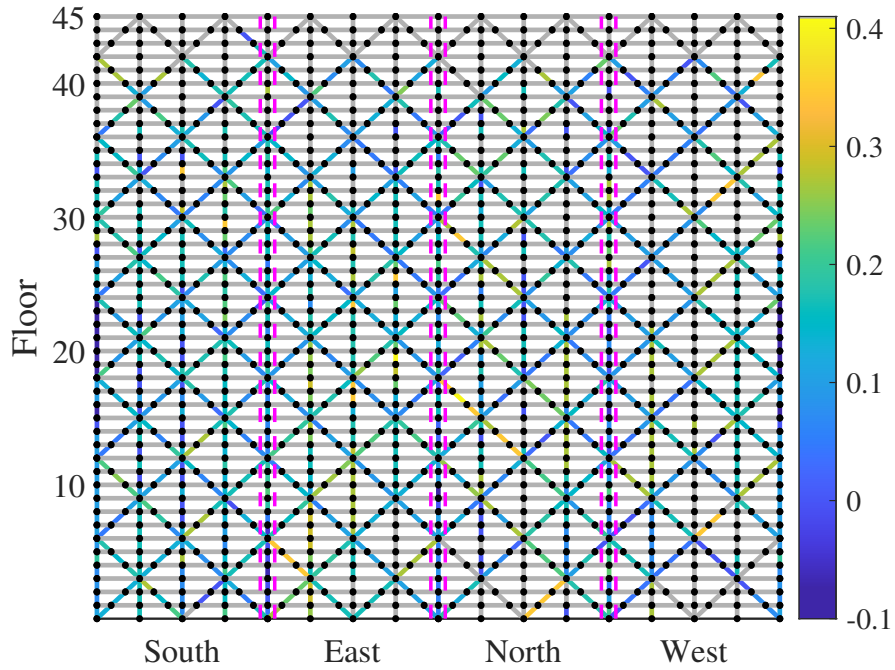


Figure 2.9: NY square steel archetype: LS1 reliability difference between AC2 and the baseline case.

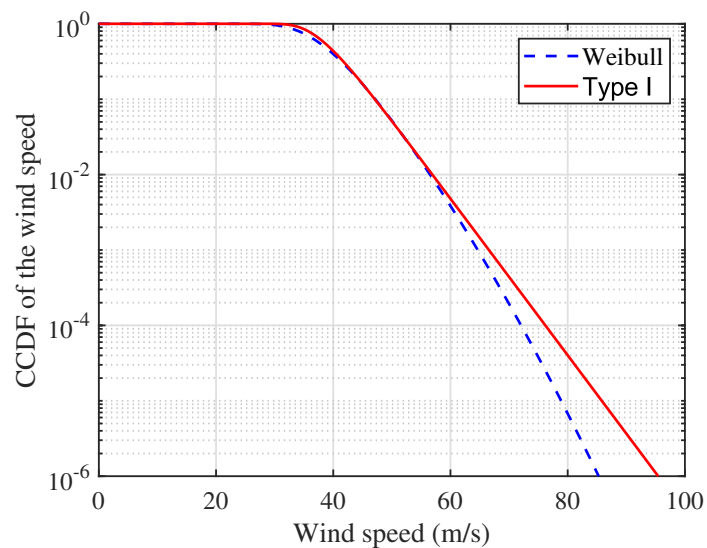


Figure 2.10: Weibull and Type I distribution curves of the largest 50-year non-directional wind speed.

the targets of Table 3.1-1. This section will explore the derivations underpinning Table 3.1-1 with the aim of finding the reasons behind these discrepancies. The derivations of this section follow those reported in [2.18].

Wind reliability model underpinning LRFD

The wind reliability model underpinning the factors used in LRFD can be best presented considering the design of steel flexural components for which the gravity load and wind actions have the same sign. In this case, the governing LRFD equation is the following:

$$0.9R_n \geq 1.2D_n + 0.5L_n + 1.0W_T \quad (2.8)$$

where R_n is the nominal strength, D_n is the nominal dead load, L_n is the nominal live load, and W_T is the nominal wind load corresponding to a 3-s gust wind speed with a return period of T -years (in ASCE 7-22, $T = 700$ years for Risk Category II structures). Defining the DCR under nominal loads as: $DCR_n = \frac{1.2D_n + 0.5L_n + 1.0W_T}{0.9R_n}$, Eq. (2.8) can be written as:

$$0.9DCR_n R_n = 1.2D_n + 0.5L_n + 1.0W_T \quad (2.9)$$

where the design scenario is for $DCR_n = 1$, i.e., when Eq. (2.8) becomes an equality.

As outlined in [2.18], the underlying limit state function of Eq. (2.8) is:

$$G(R, D, L_{apt}, W_{\max}) = R - D - L_{apt} - W_{\max} \quad (2.10)$$

where R is the random strength, D is the random dead load, L_{apt} is the random arbitrary-point-in-time live load, and W_{\max} is the maximum wind load effect to occur in a 50-year service life. As for convention, Eq. (2.10) assumes negative values when failure occurs. Equation 2.10 can be written in terms of the nominal values of the load effects and strength by first introducing the following normalized versions of the random variables R , D , L_{apt} , and W_{\max} :

- $X_1 = \frac{R}{R_n}$
- $X_2 = \frac{D}{D_n}$
- $X_3 = \frac{L_{apt}}{L_0}$
- $X_w = \frac{W_{\max}}{W_{50}}$

where L_0 is the unreduced nominal live load (with $L_n = 0.5L_0$ for all occupancies in which L_0 of ASCE 7-22 is less than or equal to 100 psf (4.78 kN/sq m) with the exception of garages or areas occupied as places of public assembly) while W_{50} is the nominal wind load effect corresponding to a 50-year return period wind speed and related to W_T as (see ASCE 7-10, C26.5-3):

$$W_{50} = \frac{W_T}{[0.36 + 0.1\ln(12T)]^2} \quad (2.11)$$

Table 2.5: Distributions of load effects and resistances

Variable	Mean	COV	Probability law
X_1	1.08	0.09	Lognormal
X_2	1.05	0.10	Normal
X_3	0.24	0.6	Gamma

In particular, for $T = 700$ years, from Eq. (2.11), $W_T = 1.6W_{50}$.

For a component with a given value of DCR_n , Eq. (2.9) and the normalized random variables introduced above, allow for the introduction of the following normalized limit state function:

$$\begin{aligned} \tilde{G}(X_1, X_2, X_3, X_w) &= \\ &= \left(\frac{1.2 + 0.25(L_0/D_n) + 1.6(W_{50}/D_n)}{0.9\text{DCR}_n R_n} \right) X_1 - X_2 - \left(\frac{L_0}{D_n} \right) X_3 - \left(\frac{W_{50}}{D_n} \right) X_w \end{aligned} \quad (2.12)$$

Equation (2.12) allows for the evaluation of the reliability of a component for a given value of DCR_n and the ratios L_0/D_n and W_{50}/D_n as long as appropriate distributions are available for X_1 , X_2 , X_3 , and X_w . From the literature, the distributions for X_1 , X_2 , and X_3 used in developing the target reliabilities of Table 1.3-1 of ASCE 7-22 can be found [2.18] and are reported in Table 2.5. In developing LRFD, X_w was defined by a Type I distribution of largest values, fitted to the 90th percentile and above the cumulative density function of W , with mean and COV of 0.90 and 0.35, respectively [2.18].

LRFD reliability and the target reliabilities of Table 1.3-1 of ASCE 7-22

Within this context, it is interesting to estimate the failure probability of an idealized steel flexural component by evaluating Eq. (2.12) through stochastic simulation and the probability distributions introduced for X_1 , X_2 , X_3 , and X_w . Equation (2.2) can then be invoked to estimate the reliability index of the component. In particular, of interest is the reliability of a component designed to exactly satisfy the LRFD scheme of Eq. (2.8), i.e., $\text{DCR}_n = 1$. In addition, the typical range for the ratio W_{50}/D_n is 0.5 to 4 while the ratio L_0/D_n is considered to range from 0 to 1 with live load reduction of 0.4 used in the calculations.

Figure 2.11 reports the variation of the reliability index as the ratios W_{50}/D_n and L_0/D_n are varied. As can be seen, for $L_0/D_n = 0$ and $W_{50}/D_n = 2$ a reliability of $\beta = 2.49$ is achieved for the component which is consistent with the “apparent reliability” results reported in [2.18] for a Risk Category II system. Interestingly, it is seen that varying the ratio L_0/D_n has little effect on the reliability (2.49 to 2.46 for L_0/D_n varying from 0 to 1 and $W_{50}/D_n = 2$), especially for higher values of the ratio W_{50}/D_n , i.e., when wind load effects dominate over dead load effects.

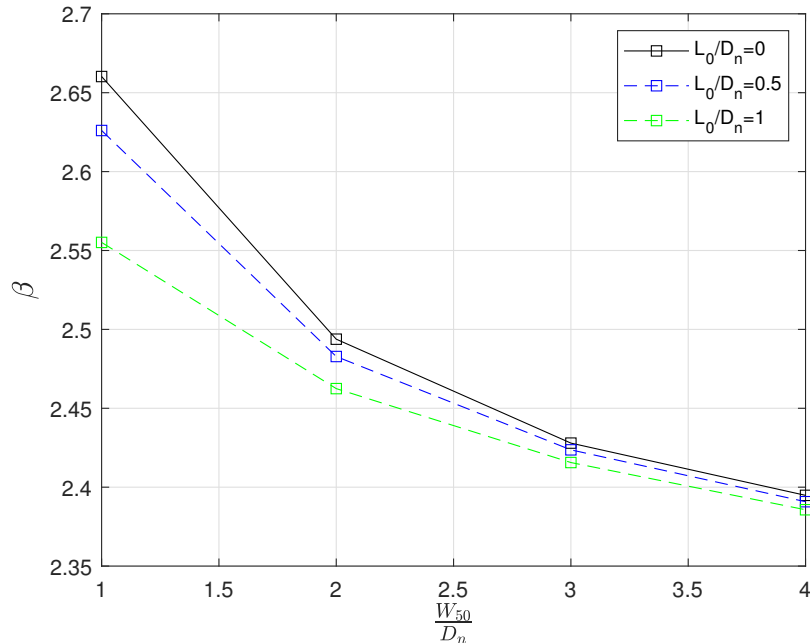


Figure 2.11: Reliability index for the simplified reliability case with W_{50}/D_n ranging from 1 to 4 and L_0/D_n ranging from 0 to 1.

Consequently, the following discussion will focus on the case $L_0/D_n = 0$ to be consistent with what can be found in literature [2.18].

The consequence of obtaining a reliability of $\beta = 2.49$ is that for analysis in which wind loads (whether in the form of ESWLs or dynamic wind loads) are developed based on 700-year return period critical loads effects (i.e., the archetype systems of this project) an implicit load factor of around 1.2 would be necessary to reach the target reliability of 3.0 of Table 1.3-1. Therefore for $W_{50}/D_n = 2$ and $L_0/D_n = 0$ a reliability of around 2.5 should be expected when using LRFD, which is generally consistent with the explicit reliability results of Section 2.2. This discrepancy was also discussed in [2.18] and traced back to a conservative choice of wind directionality factor. Nevertheless, it would seem evident that Table 1.3-1 requires clarification for use in explicit reliability analysis as the reported target values will not necessarily be obtained for components satisfying LRFD wind requirements if the wind loads are calibrated to load effects based on the return periods of the ASCE 7 wind maps.

The discussions of this section are based on distributions for X_1 , X_2 , X_3 , and X_w that were derived mainly using engineering judgment. The next section will compare results obtained from the explicit reliability analysis of Section 2.2.2 where the distributions of the random variables were estimated for the basic variables of the problem, i.e., at the level of the system parameters for which far more experimental/observational data is available. In addition, all dynamic effects (by explicitly solving the dynamic equations of motion of the system) and aerodynamic inter-

actions (by using building specific aerodynamic wind tunnel data) are explicitly captured.

2.4.2 Comparison to explicit reliability estimates

The developments of Section 2.4.1 can be used to make a direct comparison between reliability estimates based on the simplifications of Section 2.4.1 and those derived from the explicit reliability estimation framework of Section 2.1. To this end, it is useful to derive the reliability for a generic steel component for various values of the ratio W_{50}/D_n and DCR_n while fixing $L_0/D_n = 0$, i.e., absence of live loads. This is reported in Fig. 2.12 and can be used to quickly estimate the idealized reliability of a component given W_{50}/D_n and DCR_n . Using the contours of Fig. 2.12 after W_{50}/D_n and DCR_n were estimated for the NY square steel archetype, the component reliability map for the archetype is shown in Fig. 2.13(a) where a minimum reliability of 2.2 is estimated which is consistent with the minimum reliability of 2.31 estimated from the explicit reliability framework of Section 2.1 with live loads set to zero, Fig. 2.13(b). The difference between the reliabilities estimated from the explicit reliability framework of Section 2.1 and the simple model of Section 2.4.1 are reported in Fig. 2.14 where it can be observed that significant differences can be seen in the estimated reliabilities. This is to be expected as the simplified reliability analysis of Section 2.4.1, does not consider dynamic amplification in the analysis and will therefore generally overestimate the component reliability of the system as can be attested to in Fig. 2.14 where a moderate bias towards the explicit reliability analysis providing smaller estimates is seen. In addition, as mentioned, the simplified analysis is based on probability distributions for X_1 , X_2 , X_3 , and X_w that were derived mainly using engineering judgment as these variables are not basic random variables and cannot be easily estimated from experimental/observational data. This can easily lead to significant differences in the estimated reliability and demonstrates the need for models and frameworks that explicitly estimate the reliability of the system if design methods based on reliability estimates (e.g., Method 3 of the ASCE Prestandard on PBWD) are to be used. Importantly, it should be observed that, the models of Section 2.4.1 were never intended for use in design or reliability estimation of specific components in systems. Rather, they were developed for calibrating codes and are therefore only appropriate for reliability estimation under specific conditions and should be interpreted here with care. Finally, while definitely not a significant difference, the reliabilities of Fig. 2.13(a) are based on the use of a set of ESWLs as apposed to the full suite of dynamic wind loads across all wind intensities of Fig. 2.13(b).

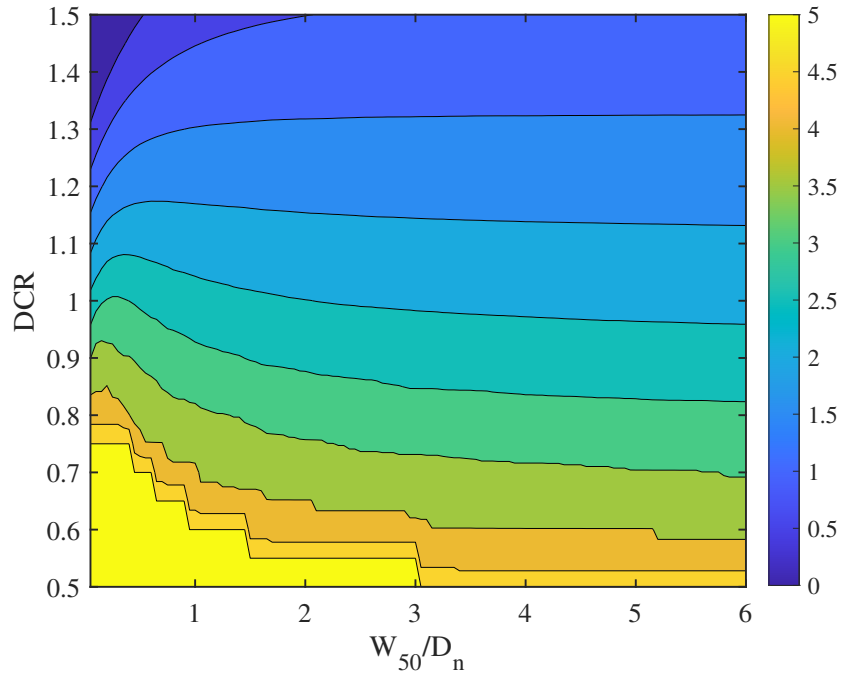
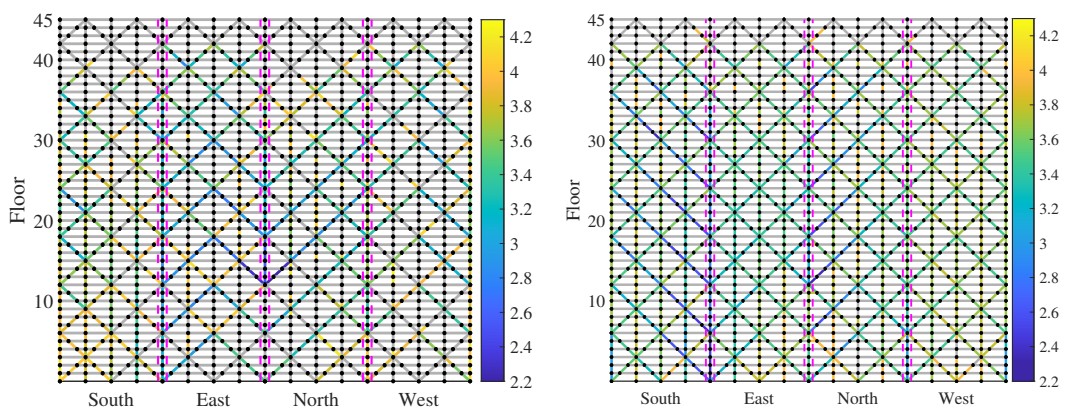


Figure 2.12: Variation of reliability with W_{50}/D_n and DCR_n for $L_0/D_n = 0$ and the simplified reliability model of Section 2.4.1.



(a) Simplified reliability

(b) WiRA reliability

Figure 2.13: Comparison between reliabilities estimated from the simplified model of Section 2.4.1 and those estimated from the WiRA framework of 2.1.

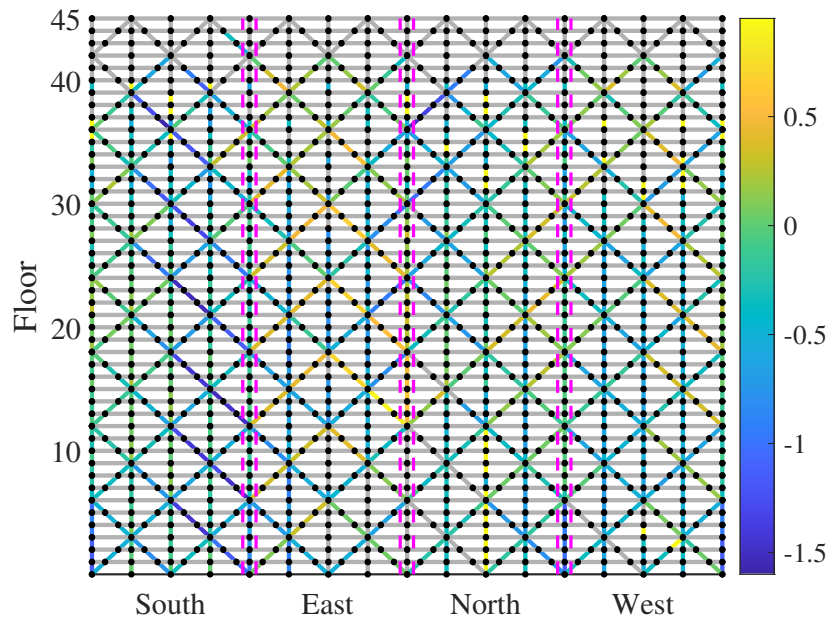


Figure 2.14: Difference between reliability estimated from the WiRA framework of Section 2.1 and the simple model of Section 2.4.1.

2.5 Concluding remarks

In this phase of the project, the underlying reasons why the apparent reliability of the MWFRS designed to comply with current LRFD requirements when using ESWL derived from building-specific wind tunnel tests and calibrated to the wind intensities suggested in ASCE 7 was investigated. To this end, two Risk Category II archetype MWFRS were considered that were subject to a careful QA/QC to ensure their representative nature. The “true” reliabilities of the two archetypes were estimated in the wind reliability modeling environment WiRA. This provided baseline component reliability estimates that were seen to be in deficit as compared to the target reliabilities suggested in ASCE 7-22 for code-compliant building systems. The sensitivity of the results to modeling choices associated with the wind hazard, including the choice of wind hazard curve, was studied and seen not to be the root cause of the deficit in reliability. Subsequently, the theory underpinning the wind reliability estimates used in calibrating LRFD was revisited. It was observed that the reliability of components designed to the wind intensities suggested in the ASCE 7 through LRFD are in deficit to the target reliabilities of Table 1.3-1 with Risk Category II systems achieving a reliability around 2.5 instead of 3.0. This is a consistent result with that reported in [2.18] where it was observed that a wind load coefficient of around 1.2 would be required if wind components designed by LRFD are to achieve the target reliability of Table 1.3-1. Interestingly, this “reduced” target reliability was inline with the “true” reliabilities of the two archetypes studied

in this Chapter. The main takeaway from the results of this Chapter is that the reliabilities of Table 1.3-1 require detailed commentary before they can be used as targets in PBWD as the wind intensities used in LRFD for defining design wind loads would appear to possibly result in systems that do not meet the targets of Table 1.3-1.

Disclaimer: The results of this chapter must be considered in light of the following limitations:

1. The reliabilities reported for the NY square steel archetype are lower than would be expected for a code-conforming building because the WiRA model of the system had a critical DCR greater than 1. If the building were redesigned, it would be expected that the reliability would be greater than 2.5 and closer to the reliabilities seen for the NY rectangular concrete core archetype.
 2. All reliability results reported were estimated using stochastic simulation and are therefore subject to inevitable statistical error associated with the use of a limited set of samples. The exact values reported should therefore be taken as representative but could be in excess or deficit of the true value.
 3. All reliability analyses carried out in this chapter do not consider epistemic uncertainty, i.e., systematic or reducible uncertainty, arising from imperfect models. This is important to clarify as building-specific wind tunnel data coupled with dynamic analysis of the system provides a representation with far lower epistemic uncertainty than, for example, the simplified models used to define Table 1.3-1. Strictly speaking, a comprehensive comparison between the target reliabilities of Table 1.3-1 and those obtained from the type of analysis outlined in this chapter should consider this difference in epistemic error.
-

Bibliography

- [2.1] American Society of Civil Engineers. *ASCE 7-22: Minimum design loads and associated criteria for buildings and other structures*. American Society of Civil Engineers (ASCE), Reston, VA, 2022.
- [2.2] S. Arunachalam and S. M. J. Spence. Reliability-Based Collapse Assessment of Wind-Excited Steel Structures within Performance-Based Wind Engineering. *Journal of Structural Engineering*, 148(9):04022132, 2022.
- [2.3] S. Arunachalam and S. M. J. Spence. An efficient stratified sampling scheme for the simultaneous estimation of small failure probabilities in wind engineering applications. *Structural Safety*, 101:102310, 2023.
- [2.4] S. Arunachalam and S. M. J. Spence. Generalized stratified sampling for efficient reliability assessment of structures against natural hazards. *Journal of Engineering Mechanics*, 149(7):04023042, 2023.
- [2.5] R. Bashor, T. Kijewski-Correa, and A. Kareem. On the wind-induced response of tall buildings: the effect of uncertainties in dynamic properties and human comfort thresholds. In *10th Americas Conference on Wind Engineering*, 2005. CD-ROM.
- [2.6] E. Bernardini, S. M. J. Spence, D.-K. Kwon, and A. Kareem. Performance-based design of high-rise buildings for occupant comfort. *Journal of Structural Engineering*, 141(10):04014244, 2015.
- [2.7] W. C. Chuang and S. M. J. Spence. A performance-based design framework for the integrated collapse and non-collapse assessment of wind excited buildings. *Engineering Structures*, 150:746–758, 2017.
- [2.8] W. C. Chuang and S. M. J. Spence. An efficient framework for the inelastic performance assessment of structural systems subject to stochastic wind loads. *Engineering Structures*, 179:92–105, 2019.
- [2.9] W. C. Chuang and S. M. J. Spence. Probabilistic performance assessment of inelastic wind-excited structures within the setting of distributed plasticity. *Structural Safety*, 80:101923, 2020.

-
- [2.10] W. C. Chuang and S. M. J. Spence. A framework for the efficient reliability assessment of inelastic wind excited structures at dynamic shakedown. *Journal of Wind Engineering and Industrial Aerodynamics*, page 104834, 2022.
- [2.11] T. G. A. Duarte, A. Arunachalam, A. Subgranon, and S. M. J. Spence. Uncertainty quantification and simulation of wind-tunnel-informed stochastic wind loads. *Wind*, 3(3):375–393, 2023.
- [2.12] B. R. Ellingwood, J. G. MacGregor, T. V. Galambos, and C. A. Cornell. Probability based load criteria: Load factors and load combinations. *Journal of the Structural Division*, 108:978–997, 1982.
- [2.13] J. Healey, S. Wu, and M. Murga. *Structural building response review. NUREG/CR1423, vol. I*. US Nuclear Regulatory Commission, Washington, DC, 1980.
- [2.14] P. A. Irwin, J. Garber, and E. Ho. Integration of wind tunnel data with full scale wind climate. In *10th Americas Conference on Wind Engineering, American Association of Wind Engineering*, page 132–135, 2005.
- [2.15] N. Isyumov, E. Ho, and P. Case. Influence of wind directionality on wind loads and responses. *Journal of Wind Engineering and Industrial Aerodynamics*, 133(1):169–180, 2014.
- [2.16] J. Judd and F. Charney. Inelastic behavior and collapse risk for buildings subjected to wind loads. In N. Ingraffea and M. Libby, editors, *Structures Congress 2015*, pages 2483–2496, April 23-25, Portland, Oregon, USA, 2015.
- [2.17] J. P. Judd. Windstorm resilience of a 10-story steel frame office building. *ASCE-ASME Journal of Risk and Uncertainty in Engineering Systems, Part A: Civil Engineering*, 4(3), 2018.
- [2.18] T. P. McAllister, N. Wang, and B. R. Ellingwood. Risk-informed mean recurrence intervals for updated wind maps in ASCE 7-16. *Journal of Structural Engineering*, 144(5):06018001, 2018.
- [2.19] A. Mohammadi, A. Azizinamini, L. Griffis, and P. Irwin. Performance assessment of an existing 47-story high-rise building under extreme wind loads. *Journal of Structural Engineering*, 145(1), 2019.
- [2.20] Z. Ouyang and S. M. Spence. A performance-based wind engineering framework for envelope systems of engineered buildings subject to directional wind and rain hazards. *Journal of Structural Engineering*, 146(5):04020049, 2020.
- [2.21] Z. Ouyang and S. M. J. Spence. Performance-based wind-induced structural and envelope damage assessment of engineered buildings through nonlinear
-

-
- dynamic analysis. *Journal of Wind Engineering and Industrial Aerodynamics*, 208:104452, 2021.
- [2.22] P. E. Pinto, R. Giannini, and P. Franchin. *Seismic Reliability Analysis of Structures*. IUSS Press, Pavia, Italy, 2004.
- [2.23] F. Sadek, S. Diniz, M. Kasperski, M. Gioffrè, and E. Simiu. Sampling errors in the estimation of peak wind-induced internal forces in low-rise structures. *Journal of Engineering Mechanics*, 130(2):235–239, 2004.
- [2.24] S. M. J. Spence and S. Arunachalam. Performance-based wind engineering: Background and state of the art. *Frontiers in Built Environment*, 8:830207, 2022.
- [2.25] A. Sukswan and S. M. J. Spence. Optimization of uncertain structures subject to stochastic wind loads under system-level first excursion constraints: A data-driven approach. *Computers & Structures*, 210:58–68, 2018.
- [2.26] P. Tabbuso, S. M. Spence, L. Palizzolo, A. Pirrotta, and A. Kareem. An efficient framework for the elasto-plastic reliability assessment of uncertain wind excited systems. *Structural Safety*, 58:69–78, 2016.
- [2.27] H. Zhang, B. R. Ellingwood, and K. J. R. Rasmussen. System reliabilities in steel structural frame design by inelastic analysis. *Engineering Structures*, 81:341–348, 2014.
-

Appendix A

Finite element model development and QA/QC

A.1 Square steel NYC

A.1.1 Modeling approach

The columns and braces of the square steel archetype are mostly wide flange W14 sections, with some corner columns at floors 1-12 assuming special W14 sections with cover plates or concrete composite sections. Beams are wide flange W18 or W24 sections with the interior beam pin-pin connected and the exterior beam fix-fix connected. Each floor is assumed to be a rigid diaphragm. The comparison between the natural frequencies of the ETABS model of the designers and the OpenSees Navigator and WiRA models of the project are reported in Table A.1. As can be seen, good correspondence is achieved between all models.

In the ETABS model, the interior gravity system (beams and gravity columns) is explicitly modeled. A rigid floor diaphragm is applied at each floor. For model development, the end length offset and P-delta effect are not considered in either the ETABS model or the WiRA model. Also, the floor is explicitly modeled in ETABS with the bending and twisting moment about the edges released. For the WiRA model, the interior beams are not explicitly modeled because of the pin-pin connections and rigid floor diaphragm assumption. In contrast, the exterior beam is explicitly modeled with fixed-fixed connections. The mass of the structural and gravity beams is concentrated at the mass center of each floor. The interior gravity columns are also not explicitly modeled as they do not provide lateral load resistance. The distributed plasticity stress resultant model is adopted to establish the finite element model. To realize this, all columns are modeled using displacement-based beam-column elements with five integration points along their lengths. Braces are modeled using truss elements and connected at each story. The floor is not explicitly modeled in the WiRA model. The mass and the weight of the floor are concentrated at the mass center of each floor.

Table A.1: NY square steel archetype: natural frequency comparison between the ETABS model of the designers and the OpenSees Navigator and WiRA models of the project (Units: Hz).

Model	1st	2nd	3rd
ETABS	0.250	0.274	0.661
OpenSees Navigator	0.2569	0.2923	0.7102
WiRA	0.2569	0.2923	0.7101

A.1.2 QA/QC: Column line response comparison

Three column lines are chosen for response comparison: two of them (C1 and C2 in the following) are located at the south face of the structure while the other is located at the west face of the structure (C3). The axial force, major bending moment, and minor bending moment of the column lines are compared between the ETABS model provided by the designers and the WiRA model. The comparison is shown in Figs. A.1 and A.3. It is noted that the force and moment are normalized by the capacity of each element along the column line. The major and minor bending responses of the column lines are similar. The normalized axial force responses show a maximum discrepancy of around 0.08.

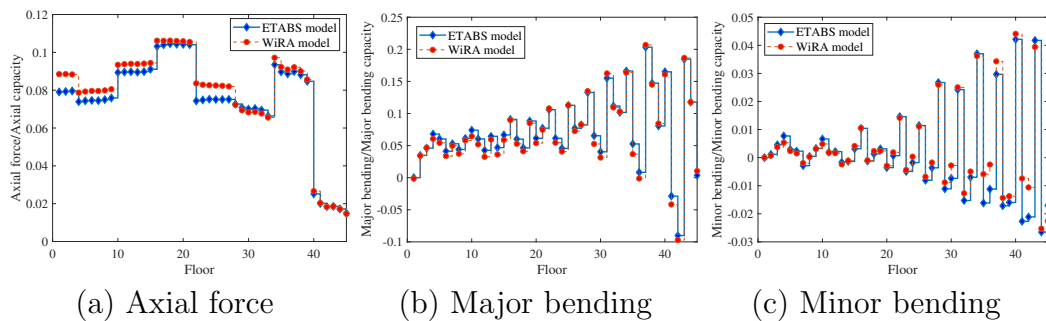


Figure A.1: Normalized response comparison for the C1 column line.

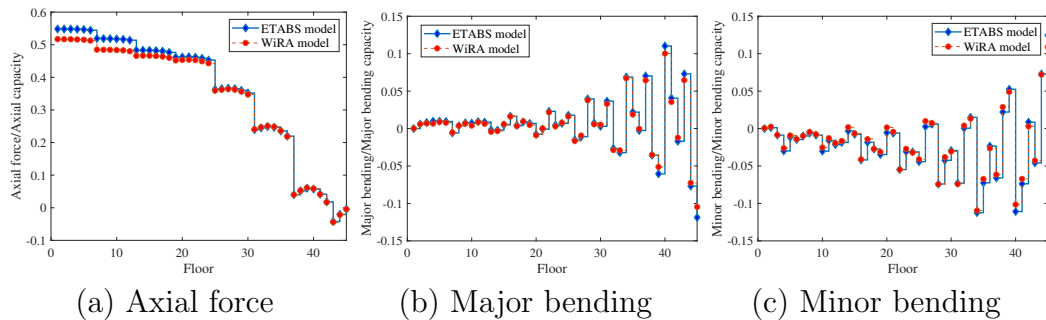
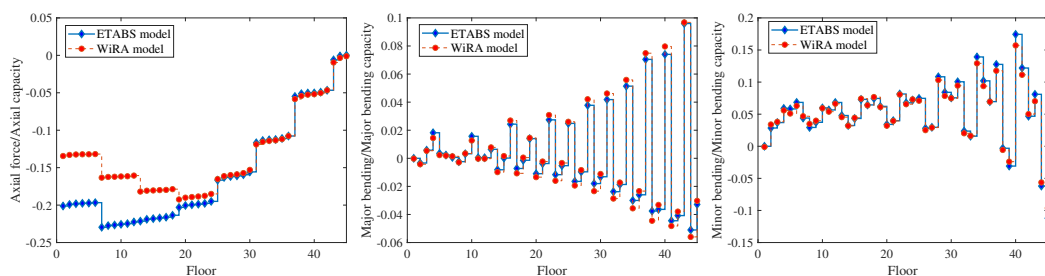


Figure A.2: Normalized response comparison for the C2 column line.



(a) Axial force (b) Major bending (c) Minor bending
 Figure A.3: Normalized response comparison for the C3 column line.

A.2 Rectangular Concrete NYC

A.2.1 Modeling approach

The NY rectangular concrete core archetype has a width of 45 meters and a depth of 30 meters. The total height is 180 meters with the height of each floor being 4 meters. In WiRA, the shear walls are modeled as equivalent columns (modeled with displacement-based beam-column elements) and rigid links (modeled with twoNodeLink elements). Coupling beams are modeled with the displacement-based beam-column elements. In the ETABS model, the shear walls are modeled using shell elements. In both the ETABS and WiRA models, each floor is treated as a rigid diaphragm with mass assumed to be concentrated at the geometric center. The shear walls have a stiffness modifier of 0.7 for both flexural and axial actions. The coupling beams have a stiffness modifier of 0.35 for flexural actions. The natural frequencies are reported in Table A.2.

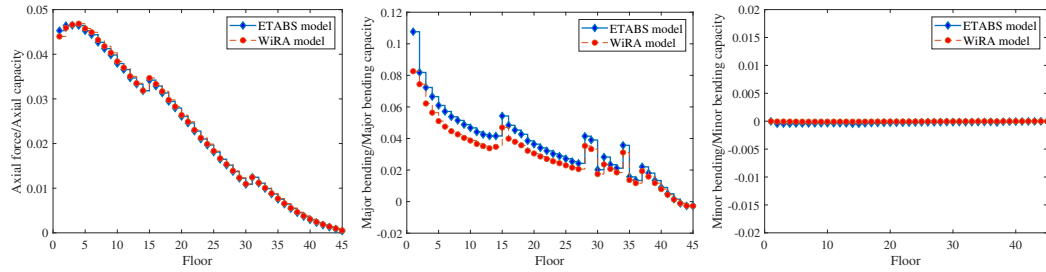
Table A.2: NY rectangular concrete core archetype: natural frequency comparison between the ETABS model of the designers and the OpenSees Navigator and WiRA models of the project (Units: Hz).

Model	1st	2nd	3rd
ETABS	0.250	0.287	0.635
OpenSees Navigator	0.2706	0.3256	0.8667
WiRA	0.2705	0.3256	0.8666

A.2.2 QA/QC: Wall line response comparison

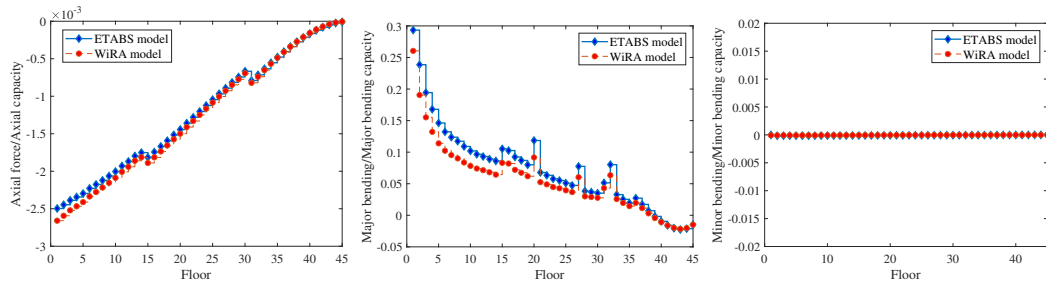
Three shear wall elevations (indicated as A1, B1, and C1 in the following) on the south face of the structure are chosen for response comparison. The axial force, major bending moment, and minor bending moment of the shear walls are compared in Figs. A.4 to A.6 for the ETABS and WiRA models. The force and moment

responses are normalized by the capacity of the shear wall. Both the axial forces and the bending moment responses show similar response trends.



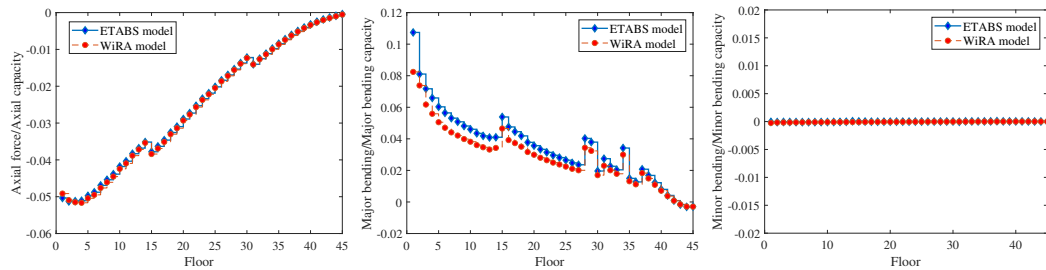
(a) Axial force (b) Major bending (c) Minor bending

Figure A.4: Normalized response comparison for the A1 shear wall.



(a) Axial force (b) Major bending (c) Minor bending

Figure A.5: Normalized response comparison for the B1 shear wall.



(a) Axial force (b) Major bending (c) Minor bending

Figure A.6: Normalized response comparison for the C1 shear wall.

Appendix B

Stochastic wind load model and the Miami archetype

B.1 Wind load calibration

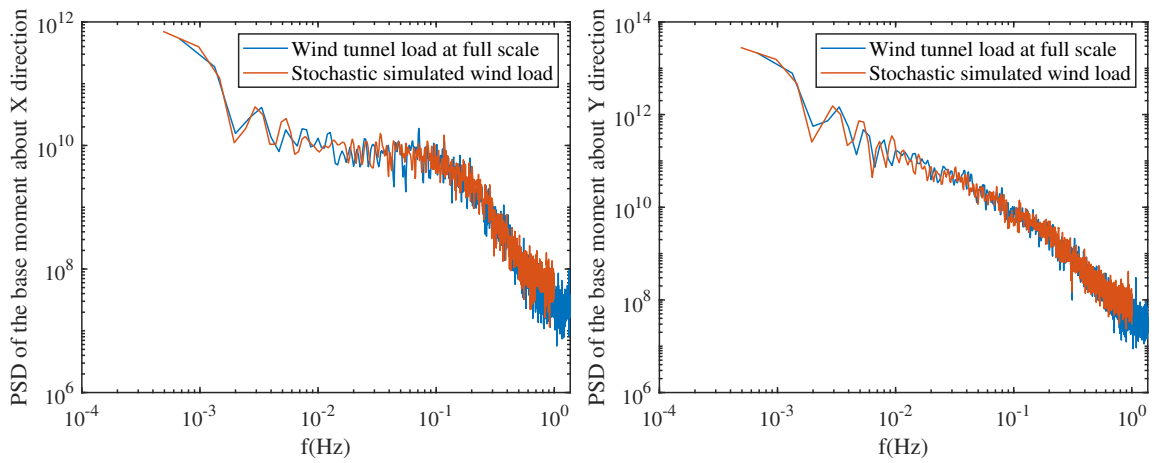
From Fig. 1.11, it is clear that the biggest discrepancy between the peak DCRs estimated from the non-Gaussian stochastic wind load model and the wind tunnel realization of the dynamic wind loads occurs for a wind direction of 200° . To provide confidence in the calibration process, Figs. B.1 and B.2 report the comparison between the power spectral density (PSD) and cross power spectral density (CPSD) estimated from the wind tunnel data (the target) and those estimated from a realization of the calibrated non-Gaussian stochastic wind load model. As can be seen, very good correspondence is achieved.

Concerning the capture of the non-Gaussian features, Fig. B.3 reports the comparison of the skewness and kurtosis between the wind tunnel data (the target) and those estimated from the calibrated non-Gaussian stochastic wind load model for a wind direction of 200° . In particular, Fig. B.3 reports the comparison in terms of each component of the wind load vector. From Fig. B.3, the capability of the stochastic wind load model to capture the non-Gaussian features can clearly be seen. In addition, it is interesting to observe the strong non-Gaussian features of the floor loads.

Similar results to those shown in Figs 1.11 to B.3 were obtained for all wind directions therefore providing confidence that the non-Gaussian stochastic wind load model adopted in this project was well calibrated to the wind tunnel data representing the target process.

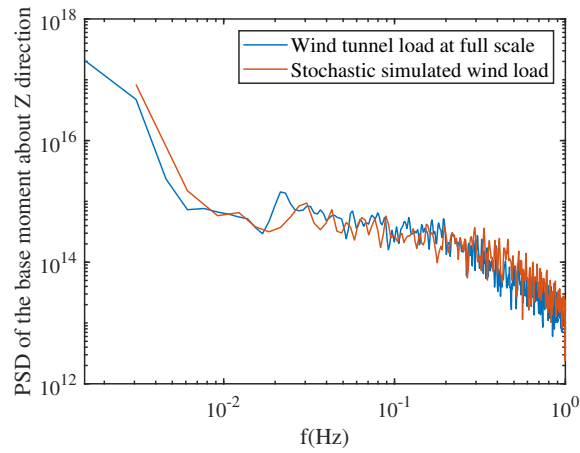
B.2 Discussion on the Peak DCR

For the wind direction of 200° , Fig. 1.11 shows a large difference between the peak DCR obtained from the application of the wind tunnel realization of the wind load



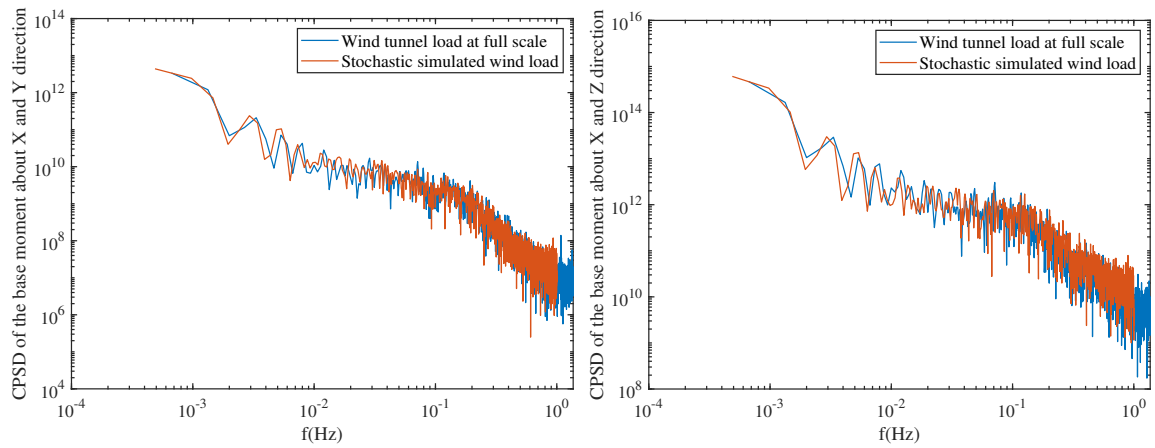
(a) Moment about the X axis.

(b) Moment about the Y axis.



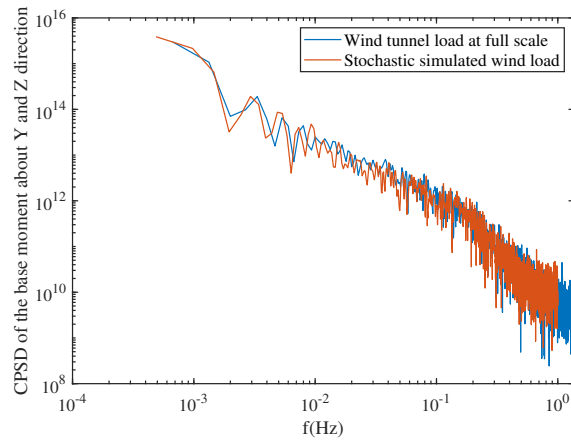
(c) Moment about the Z axis.

Figure B.1: Miami rectangular steel archetype: PSD comparison between the aerodynamic base moments for a wind direction of 200° .



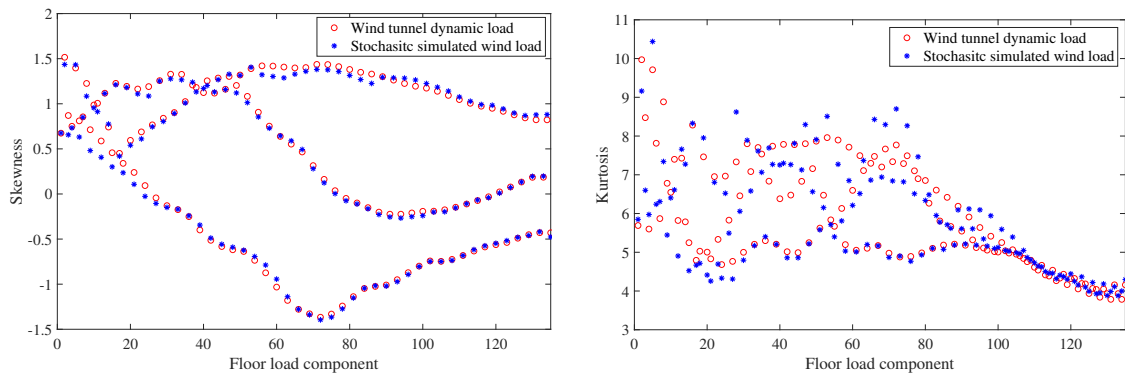
(a) X-Y Moment interaction.

(b) X-Z Moment interaction.



(c) Y-Z Moment interaction.

Figure B.2: Miami rectangular steel archetype: CPSD comparison between the aerodynamic base moments for a wind direction of 200° .



(a) Skewness of the floor loads.

(b) kurtosis of the floor loads.

Figure B.3: Comparison between the target and simulated skewness and kurtosis of the floor loads.

process and the maximum peak obtained from the application of 100 realizations of the calibrated non-Gaussian stochastic wind load model.

To shed light on the causes of this difference, Fig. B.4 reports the DCR time history for the wind demand and the critical projection for the component experiencing the maximum DCR under the wind tunnel realization of the wind load process. Both the response under the wind tunnel realization and the stochastic load realization producing the largest DCR are shown. As can be seen, notwithstanding how 100 stochastic wind load realizations were generated, the wind tunnel realization produces a significantly larger peak. It is interesting to observe that both the peak DCR produced by the wind tunnel load realization and stochastic load realization are similar to the peaks discussed in Section 1.2.2 for the NY square steel archetype. Indeed, as illustrated in Fig. B.5, the PSDs of the response histories show a significant peak in energy around the first natural frequency of the MWFRS. However, the resonance produced by the wind tunnel realization was significantly larger than that produced by the 100 realizations of the non-Gaussian stochastic wind load model notwithstanding the successful calibration results reported in Section B.1. Similar results were seen for the other wind directions where the peak DCR of the wind tunnel realization was larger than those of the 100 realizations of the stochastic wind load model.

All things even, it would be expected that the peak DCRs from the wind tunnel realization of the stochastic load process would roughly be above the mean DCR of the 100 stochastic realizations 50% of the time. However, as is clearly evident from Fig. 1.11, this is not the case. Because the calibration of the non-Gaussian stochastic wind load model did not seem to present any errors, as illustrated in Section B.1, it was concluded that the non-Gaussian stochastic wind load model adopted in this project may not be always cable of completely representing the “true” stochastic wind load process. The further investigation of this issue is beyond the scope of this project.

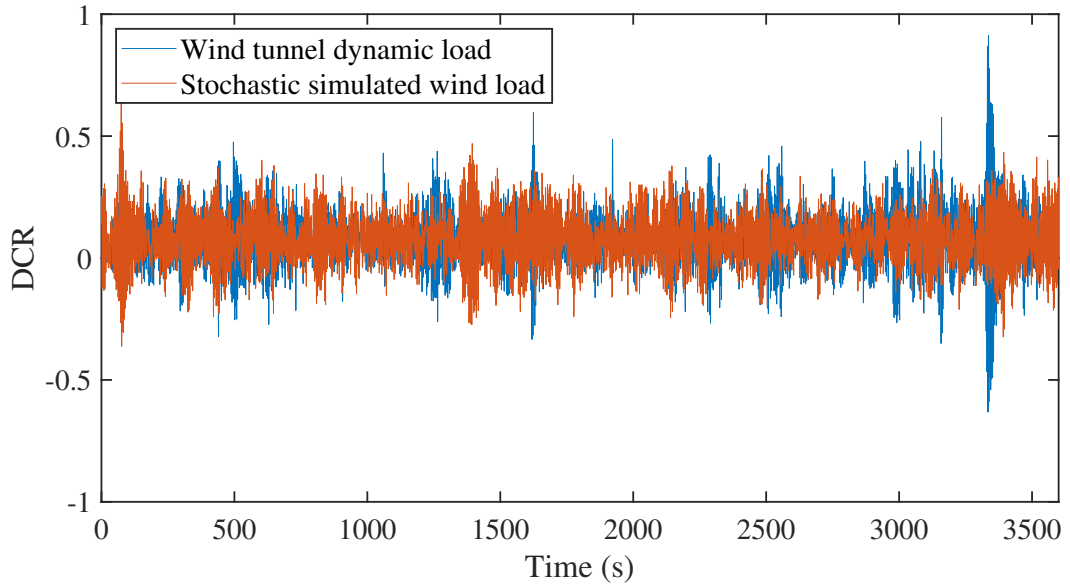


Figure B.4: Critical wind demand DCR time history for the component experiencing the maximum DCR under the dynamic wind tunnel load.

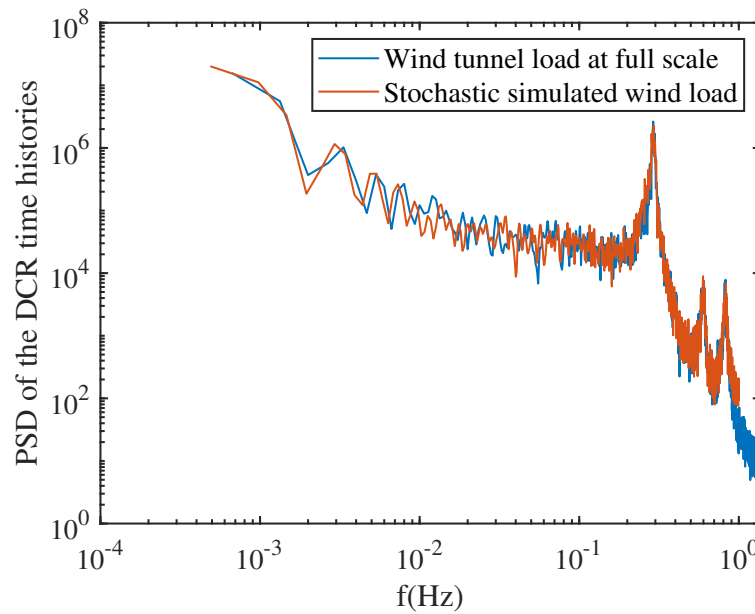


Figure B.5: PSD of the critical wind demand DCR time histories of Fig. B.4.